DOE/PC/90182--T22

APPENDIX 3

MEASUREMENTS OF GRANULAR FLOW DYNAMICS WITH HIGH SPEED DIGITAL IMAGES

By

JINGEOL LEE

A DISSERTATION PRESENTED TO THE GRADUATE SCHOOL
OF THE UNIVERSITY OF FLORIDA IN PARTIAL FULFILLMENT
OF THE REQUIREMENTS FOR THE DEGREE OF
DOCTOR OF PHILOSOPHY

UNIVERSITY OF FLORIDA

1994

Appendix 3: Lee (1994) Ph.D. Thesis

DISCLAIMER

ACKNOWLEDGMENTS

The author would like to gratefully acknowledge his advisor and supervisory committee chairman, Dr. Jose C. Principe, for his advice and encouragement during the course of graduate studies.

The author would like to express his deep appreciation to Dr. Daniel M. Hanes for his guidance and support in the course of this work. He is also grateful to Dr. John M. M. Anderson for helpful discussions and suggestions.

The author is also greatly indebted to the other members of his supervisory committee, Dr. Fred J. Taylor and Dr. Robert J. Thieke.

The author would like to thank all the members who have worked together in Granular Flow Laboratory. In particular, thanks are due to a good friend, David Larocca, for his help in laboratory experiments. He also thanks John Fisher for helpful discussion about MACE filter.

Finally, the author would like to thank his wife for her support and patience throughout these difficult years.

TABLE OF CONTENTS

APPENDICES

Abstract of Dissertation Presented to the Graduate School
of the University of Florida in Partial Fulfillment of the
Requirements for the Degree of Doctor of Philosophy

MEASUREMENTS OF GRANULAR FLOW DYNAMICS WITH HIGH SPEED DIGITAL IMAGES

By

JINGEOL LEE

December, 1994

Chairman: Dr. Jose C. Principe
Major Department: Electrical Engineering

The flow of granular materials is common to many industrial processes. This dissertation suggests and validates image processing algorithms applied to high speed digital images to measure the dynamics (velocity, temperature and volume fraction) of dry granular solids flowing down an inclined chute under the action of gravity. Glass and acrylic particles have been used as granular solids in our experiment.

One technique utilizes block matching for spatially averaged velocity measurements of the glass particles. This technique is compared with the velocity measurement using a optic probe which is a conventional granular flow velocity measurement device.

The other technique for measuring the velocities of individual acrylic particles is developed with correspondence using a Hopfield network. This technique first locates the positions of particles with pattern recognition techniques, followed by a clustering technique, which produces point patterns. Then, correspondence between successive point pat-

terns is solved by a Hopfield network for the velocity measurements of individual particles. The velocity measurements are refined to the subpixel resolution by the variance normalized correlation with interpolation in both glass and acrylic particles. Also, several techniques are compared for particle recognition: synthetic discriminant function (SDF), minimum average correlation energy (MACE) filter, modified minimum average correlation energy (MMACE) filter and variance normalized correlation. We propose an MMACE filter which improves generalization of the MACE filter by adjusting the amount of averaged spectrum of training images in the spectrum whitening stages of the MACE filter.

Variance normalized correlation is applied to measure the velocity and temperature of flowing glass particles down the inclined chute. The measurements are taken for the steady and wavy flow and qualitatively compared with a theoretical model of granular flow. Also, the volume fraction measurement of flowing acrylic particles is taken and methodologically compared with the Drake's manual measurement.

CHAPTER 1
INTRODUCTION

'A granular material is a collection of a large number of discrete solid particles' (Campbell 1990 p. 57). Gravity driven granular flows down inclined surfaces occur in geophysical flows such as snow avalanches and rock landslides and in various industrial situations such as coal and mineral processing and many chemical and pharmaceutical industries. The interstices between the particles in the granular materials are filled with a fluid such as air or water, which means that a granular flow is multiphase process. However, if the particles are closely packed, the particles alone will play dominant role in momentum transport within the material, in which interstitial fluid effects are negligible.

A granular material may behave as either an elastic solid or a fluid depending on the local stress conditions. A granular material can support the large loads of building foundations with its elastic solid behavior, in which much of the load is supported across frictional bonds between particles. A granular material begins to flow when enough of bonds have been overcome. The initial failure will show many-particle blocks moving relative to one another along shear bands that roughly follow stress characteristics through the material. Particles will stay in contact and interact frictionally with their neighbors over long periods of time if the motion occurs slowly. This is the quasi-static regime of the granular flow.

The other extreme is the rapid-flow regime, which, as the name implies, is high-speed flows far beyond the initial failure. Each particle moves freely and independently of even its nearest neighbors instead of moving in many-particle blocks. This rapid-flow regime evolves naturally from the quasi-static regime if the motion is rapid enough to transfer enough energy to the particles that neighbor the slip lines to break them free of their parent blocks; in this way the slip regions grow until every particle in the granular material is moving independently. In the rapid-flow regime, the velocity of each particle may be composed of the mean velocity of the bulk material and an apparently random component to describe the motion of the particle relative to the mean. Due to the strong analogy between the random motion of the granular particles and the thermal motion of molecules in the kinetic-theory picture of gas, the mean square value of the random velocity is commonly referred to as the granular temperature or simply temperature. The granular temperature is defined as $T = \frac{1}{3}(\langle u'^2 \rangle + \langle v'^2 \rangle + \langle w'^2 \rangle)$ where u', v', w' are instantaneous velocity fluctuations, and $\langle\ \rangle$ represents an appropriate average. Thus, T represents the energy per unit mass contained in the random motions of the particles.

The generation of the granular temperature can be attributed to the two mechanisms. The first mechanism is described by interparticle collisions. When two particles collide, their resultant velocities will depend on their initial velocities, the angle at which two particles collide, the surface friction at the point of contact, and other factors that may affect the geometry of collision impulse. Thus, even though the particles initially move with the mean velocities according to their positions within the velocity field, their resultant velocities will contain apparently random velocity components. It is noticeable that the magnitude of the random velocities generated in this mode will be proportional to the rel-

ative velocities of the particles at the time of impact and hence must, in an averaged sense, be proportional to the mean velocity gradient within the material. The second mechanism is described by the random particle velocities. A particle moving parallel to the local velocity gradient will pick up an apparently random velocity that is roughly equal to the difference in the mean velocity between its present location and the point of its last collision. The magnitude of the random velocities generated in this mode will also be proportional to the local velocity gradient. However, unlike the collisional temperature generation, this streaming mechanism can only generate one component of random velocity which lies in the direction perpendicular to the mean velocity gradient. Consequently, the temperature generated in this mode will be anisotropic with its largest component in the direction of mean motion. Collisional temperature generation will dominate at dense particle packings when particles can not move far between collisions, and streaming temperature generation will dominate at loose particle packings when collisions are infrequent. The granular temperature is perhaps the single most important characteristic for understanding the behavior of rapid granular flows.

The source of all the energy is the work done on the granular material from the outside, either by body forces such as gravity or through the motion of the system boundaries. Shear work (the product of the shear stress and the velocity gradient) performed on the granular material converts some of the kinetic energy of the mean motion into granular temperature. On the other hand, the granular temperature is dissipated into real thermodynamic heat by the inelastic collisions. Thus, the balance between the temperature generation by shear work and its dissipation by collisional inelasticity determines the magnitude of the granular temperature.

While the above describes the global energy path through the granular system, the magnitude of the granular temperature in neighboring area may affect the local value. This is a conduction-like process and analogous to the thermodynamic conduction in a gas. As a particle follows its random path through the material, it carries its random kinetic energy with it. When two particles collide, they exchange some of their random kinetic energy, which results in a diffusion of granular temperature through the material. As its thermodynamic counterpart, granular temperature will be conducted along its gradients.

The capability to predict the flow behavior of dry granular solids and multiphase flow with solid components would provide a basis for the improvement of solids processing plant efficiency. Theoretical and experimental studies of flowing granular material behaviors were performed in the last two decades (Savage 1979; Jenkins and Savage 1983; Hanes and Inman 1985; Johnson et al. 1990; Drake 1991). The studies addressed are the flow depth, the profiles of volume fraction, the velocity and the fluctuating velocity (temperature) versus inclination, flow rate, and position along the chute. One of the challenges in experimental studies is that there are no standard means of measuring the local velocity of granular materials. Savage (1979) used fiber optic probes to measure the local time averaged velocity of flowing spherical polystyrene beads. Patrose and Caram (1982) and McCardle (1993) also used fiber optic probes to measure the local time averaged velocity and local concentration of flowing glass particles. Drake (1991) manually analyzed images on film to measure the velocities and spins of individual cellulose acetate spheres. Xie et al. (1989) employed a charge transducer to measure the velocity and a capacitance transducer to measure the volumetric concentration of flowing fine silicate sand and polypropylene plastic granules.

The objective of this dissertation is to suggest and validate image processing algorithms applied to high speed digital images to measure the dynamics (velocity, temperature and volume fraction) of dry granular solids flowing down an inclined chute under the action of gravity. Measurement of either local average velocities, or individual particle velocities would represent a major advance in understanding the dynamics of flowing granular materials. We have taken advantage of an ongoing research project studying the flow of nearly elastic glass spheres. The choice of these particles is made as an approximation of the behavior of an ideal granular material. Glass spheres provide an excellent model of a nearly elastic, frictionless, granular material. However, the optical characteristics of glass lead to very poor image quality: since glass particles are highly reflective and somewhat transparent, the brightness pattern of glass particles in a dense flow changes in time depending on the relative position of neighboring particles and light sources. Accordingly, it is difficult to recognize glass particles by visual inspection or image processing. Therefore, we are faced with the particularly challenging task of extracting information from low quality images.

Laboratory tests are conducted in a flow simulation system which consists of a inclined chute with transparent side walls, a conveyer for particle recirculation, an upper hopper for granular storage and a lower hopper for guiding the discharge to the conveyer. The chute is 4 m long, 0.46 m tall, and the width is adjustable from 0 to 25 cm in 2.5 cm increments. The angular range which the chute is to be operable in is 0 to 35 degree. Mass flow rate is controlled by an adjustable gate located between the upper hopper and the entrance of the chute.

We have used glass and acrylic particles of 3 *mm* in diameter as granular solids for our experiment. The acrylic particles are used to develop a method for measuring the velocities of flowing particles with higher quality images: the image quality improves to the extent that visual particle recognition becomes relatively easier and brightness patterns among particles are consistent.

Images have been obtained on a system which takes digital video images up to 1000 frames/ sec with 192 by 239 resolution. The images have been taken from the side wall about 0.8 m upstream and from the top of the chute about 1.7 m upstream of the chute outlet.

Chapter 2 contains a review of major current approaches to image motion, and averaged velocity measurement of flowing glass particles with variance normalized correlation is discussed. Chapter 3 introduces velocity measurements of individual acrylic particles, which locates particles and makes particle correspondence between two successive images using a Hopfield network. Chapter 4 qualitatively compares the experimental velocity and temperature profile measurements of flowing glass particles with a theoretical model (Richman and Marciniec 1990) of granular flow. Also, the volume fraction measurement of flowing acrylic particles is discussed. Chapter 5 concludes this dissertation with results of dynamics measurement of glass and acrylic particles flowing down the inclined chute. Appendices summarize the imaging system, and developed programs are listed functionally.

CHAPTER 2
VELOCITY MEASUREMENT OF FLOWING GLASS PARTICLES

Review of Major Current Approaches to Image Motion

Most of the current approaches for the measurement of image motion deal with 2-dimensional motions in the image plane and can be classified depending on the choice of a measurement: (1) use of brightness variations over space and time to measure instantaneous image velocities, i.e., gradient-based techniques (Horn and Schunck 1981; Schunck 1989); (2) measurement of displacement of local image pattern or primitive image tokens between successive frames of a sequence, i.e., correlation - based matching techniques (Burt et al. 1982; Glazer et al. 1983) and symbolic-token based matching techniques (Prager and Arbib 1983); (3) measurement of the spatio-temporal energy of the image brightness function in a local area to determine image motion, i.e., spatio-temporal energy model (Adelson and Bergen 1985; Watson and Ahumada 1985; Heeger 1987; Daugman 1989; Tsao and Chen 1991); and (4) update of displacements based on gradient search, i.e., recursive displacement estimation (Musmann et al. 1985).

Gradient - Based Techniques

This approach is based on the assumption that a patch of uniform brightness in the image does not change with time. This can be mathematically stated as

$$i(x, y, t) = i(x + u\delta t, y + v\delta t, t + \delta t) \tag{2.1}$$

where $i(x, y, t)$ is the brightness at time t for image location (x, y), $u(x, y)$ and $v(x, y)$ are the x and y component of velocity, and δt is length of time interval. Optical flow is the velocity field in the image plane that arises due to the projection of moving patterns in the scene onto the image plane. The optical flow is modeled by the optical flow constraint equation which is derived from above equation taking the limit as $\delta t \rightarrow 0$

$$\frac{\partial i}{\partial x}u + \frac{\partial i}{\partial y}v + \frac{\partial i}{\partial t} = 0 \tag{2.2}$$

which models the interaction between the velocity field, (u, v) and the local changes in space and time of the image brightness $i(x, y, t)$.

Matching Techniques

The measurement of motion from a discrete image sequence is usually based on identifying corresponding image events from successive frames. This is called the correspondence problem and leads to a matching approach, i. e., one in which image events from successive frames are matched with each other. There are two kinds of matching techniques that are commonly used: correlation based techniques and symbolic token matching techniques.

A general statement of the local correlation between images is

$$R(m, n) = \sum_x \sum_y f(x, y)\, w(x-m, y-n) \tag{2.3}$$

where $w(x, y)$ is the mask and $f(x, y)$ is the image region coincident with $w(x, y)$. In order to estimate the displacement in the location x, y, a block of image indexed by x, y is taken from preceding frame and correlated with current frame in a search area to find the best match.

The symbolic token matching technique uses symbolic representation of geometric structure in the image as the basis for matching such as points or edges. This structure may be easily distinguishable and is likely to be stable over several image frames. With appropriate representation, it is possible to find match even for rotational or scale change. Also, increasing reliability and reducing computational complexity can be accomplish by suitable representation.

Spatio-Temporal Energy Model

The spatio-temporal energy models for motion analysis are based on the fact that the visual signal is a function of (x, y, t). Let $i(x, y, t)$ be a continuous image in space and time and $I(\omega_x, \omega_y, \omega_t)$ be its 3-D spatio-temporal Fourier transform taken over the spatio-temporal aperture $[X, Y, T]$:

$$I(\omega_x, \omega_y, \omega_t) = \int_X \int_Y \int_T i(x, y, t)\, e^{-i(\omega_x x + \omega_y y + \omega_t t)}\, dx dy dt \tag{2.4}$$

Let $\bar{v} = (u, v)$ is the local image velocity. Uniform motion $\bar{v}$ implies that for all time intervals δt,

$$i(x, y, t) = i(x + u\delta t, y + v\delta t, t + \delta t) \tag{2.5}$$

Taking the 3-D spatio-temporal Fourier transform of both sides, and applying the shift property, gives

$$I(\omega_x, \omega_y, \omega_t) = e^{i(\omega_x u\delta t + \omega_y v\delta t + \omega_t \delta t)} I(\omega_x, \omega_y, \omega_t) \tag{2.6}$$

The above equation is true only if $I(\omega_x, \omega_y, \omega_t) = 0$ for $\omega_x u + \omega_y v + \omega_t \neq 0$. This means that $I(\omega_x, \omega_y, \omega_t)$ is non-zero only on the inclined spectral plane defined by

$$\omega_x u + \omega_y v + \omega_t = 0 \tag{2.7}$$

If the motion of a small region of an image may be approximated by translation in the image plane, the velocity of the region may be computed in the frequency domain by finding the plane in which all the power resides using Gabor filters. The Gabor filter is a sine wave multiplied by a Gaussian window, by which it is localized in the space and frequency domain.

Recursive Displacement Estimation Algorithm

In recursive estimation algorithm, it is assumed that an initial estimate of displacement vector $\overline{D_i}$ is used to produce a new improved estimate $\overline{D}_{i+1}$ according to

$$\overline{D}_{i+1} = \overline{D}_i + \overline{U}_i \tag{2.8}$$

where U_i is the so-called update term of iteration i. Knowing $\overline{D}_i$ as a function of the displaced frame difference (DFD)

$$DFD(x, y, \overline{D}_i) = i_k(x, y) - i_{k-1}(x - dx_i, y - dy_i) \tag{2.9}$$

can be used as a criterion for calculating the estimate $\overline{D}_{i+1}$. This algorithm attempts to minimize the squared value of the displaced frame difference recursively using the gradient search.

$$\overline{D}_{i+1} = \overline{D}_i - \frac{1}{2}\varepsilon \nabla_{\overline{D}_i} [DFD(x, y, \overline{D}_i)]^2 \tag{2.10}$$

where $\nabla_{\overline{D}_i}$ is the gradient operator with respect to $\overline{D_i}$ and ε is a positive constant. The choice of ε requires a compromise between convergence speed and misalignment. This algorithm converges to the solution for displacement after several iteration.

Applicability of the Major Current Approaches to Velocity Measurement of Granular Flow

As discussed earlier, glass particles are highly reflective and somewhat transparent. The brightness pattern of glass particles changes abruptly in some locations between successive frames due to reflections from neighboring particles, whereas all the approaches described above require the maintenance of brightness pattern across frames.

In the gradient model, temporal sampling must be shorter than the scale of time over which the velocity field changes, which conflicts with the fact that the image brightness pattern in the image sequence must evidence a sufficient phase shift to be measured accurately. Another drawback of the gradient model with real images.is that the brightness pattern has to be smooth to the extent that its gradient must be well defined. For these reasons, it is difficult to apply the gradient model to real images. On the other hand, the high speed images are noisy due to the image intensifier multiplication process in the camera. Gradient estimate is sensitive to the noise because it is approximated by the difference of brightness values of two neighboring pixels in the horizontal and vertical directions. Moreover, the typical particle image size of 12 pixels in diameter is relatively small, and some particles show bright spots due to the reflections, which makes it difficult to define the gradients in glass particle images. The experiments with the gradient model showed that the model is not applicable to our problem due to the aforementioned reasons.

The spatiotemporal model estimates motion using a family of Gabor-energy filters. In order to apply this model to images, the image motion must be steady in direction during the analysis time. However, the direction of particle motion in a granular flow changes in time due to collisional interactions. Thus, the spatiotemporal model is not applicable to our problem.

The recursive displacement estimation algorithm uses a gradient search to get the image motion by minimizing the displaced frame difference (DFD). It is expected that this method will provide a valid solution to our problem if the DFD is modified to handle image blocks as in the correlation technique. However, this method has not been tested.

In addition to the problems the gradient model poses for our images that are mentioned above, the gradient model produces the velocity measurements at every pixel. However, velocity measurement with a resolution equal to the particle size is sufficient for our application. Accordingly, we are proposing the matching techniques for velocity measurement of granular flow; i.e., the correlation-based technique for glass particles to cope with the image problem and the symbolic-token based matching technique for acrylic particles taking points associated with locations of each particle as the symbolic representation for the matching.

Variance Normalized Correlation

As mentioned earlier, the brightness pattern of glass particles changes abruptly in some locations between successive frames due to inter-particle reflections. Methods that use image data globally to cope with such problems have to be applied, which leads to the application of the block matching technique. There are different methods to evaluate a match between two images (Rosenfeld and Kak 1976). Among them, correlation is a well known technique which is robust in noisy environment. The basic idea to estimate displacements in two successive images with the correlation is to subdivide the images into small blocks (masks) and to take a mask from a preceding frame, which contains a template and to find the best match in a search area of the current frame. There are some vari-

ations of this technique such as direct correlation, mean normalized correlation, variance normalized correlation, Laplace filtered correlation and binary correlation. Burt et al. (1982) did a comparative study and showed that the best performance was obtained with the variance normalized correlation even though it is the most expensive in computation time. The variance normalized correlation is defined as

$$r(m,n) = \frac{\sum_x \sum_y [f(x,y) - \bar{f}]\,[w(x-m,y-n) - \bar{w}]}{\left[\sum_x \sum_y [f(x,y) - \bar{f}]^2 \sum_x \sum_y [w(x-m,y-n) - \bar{w}]^2\right]^{1/2}} \qquad (2.11)$$

where $\bar{w}$ is the average intensity of the mask, $\bar{f}(x,y)$ is the average value of $f(x,y)$ in the region coincident with $w(x,y)$, and the summations are taken over the coordinates common to both f and w. The $r(m,n)$ ranges from -1 and 1, independent of scale changes in the amplitude of $f(x,y)$ and $w(x,y)$. The mask size and shape strongly influence the success of correlation matching. The pattern within the mask may not be distinctive and multiple false matches would result with too small a mask. Alternatively, differences in motion within neighboring image regions may not be resolved with too large a mask.

The two successive images of flowing glass particles in Fig. 2-1 are used to illustrate the applicability of variance normalized correlation. The image on the left hand side precedes the image on the right hand side by a sampling time of 1 msec. The image size is 96 by 119 pixels. The camera is tilted such that the chute base is parallel to the horizontal edge of images. Particles move leftward in this setup. Since particles have the same spherical shapes and are densely packed, the resultant somewhat periodic brightness pattern

may cause ambiguities in the correlation. Thus, the images are taken fast enough to guarantee that the maximum displacement is within a particle diameter, and the search area of each mask on the order of a particle diameter is restricted within the particle size. Fig. 2-2 shows the brightness pattern in the image area from 50 to 69 pixels vertically and from 80 to 99 pixels horizontally with upper left origin in the two successive frames, which are displaced 1 or 2 pixels to left with respect to the top image with visual inspection. Correlation is applied to the center area of the image in Fig. 2-2 using a mask of 13 by 13 pixels considering that the typical particle diameter is 12 pixels. The result is plotted in Fig. 2-3, in which the mask is shifted from where it was in the preceding frame 4 pixels to the left and 5 pixels up and down, respectively. The viewpoint in Fig. 2-3 is 37.5 degrees from horizontal and 30 degree in elevation. The right most vertical line corresponds to no horizontal shift of the mask and the center horizontal line corresponds to no vertical shift. The location of the peak in Fig. 2-3, which corresponds to the displacement at the center area of Fig. 2-2, is consistent with the visual inspection.

The above mentioned method is applied to the total image in Fig. 2-1. The image area is subdivided into masks of 13 by 13 pixels and each mask from the image on the left hand side is matched with the image on the right hand side in the search area using the aforementioned method. Fig. 2-4 shows the resultant displacement field over the total image area. A correlation threshold of 0.75 is used to get valid estimates, which means that only displacement measurements with the corresponding correlation value greater than the threshold are considered as the valid measurements. The same threshold will be used later for the comparison of correlation values with a sample rate decreased. The displacements at three locations in lower left are 1 pixel/ frame and rest are 2 pixels/ frame

horizontally. Since a particle whose physical diameter is 3 mm occupies 12 pixels in the image and the images are taken with the sampling time of 1 msec, one pixel displacement corresponds to the velocity of

$$3mm/12pixels \times 1pixel \times 1/0.001\,\mathrm{sec} \;=\; 25cm/\mathrm{sec}.$$

Accordingly, the horizontal velocities at the 3 lower left locations are 25 cm/ sec and the rest are 50 cm/ sec. In other words, velocity measurement resolution is 25 cm/ sec, which is quite large considering typical velocities of glass particles flowing down the inclined chute.

As means of improving the resolution, a lower sampling rate and interpolation of the correlation are tried. The sampling rate can be decreased to the extent that the displacement is within one particle diameter. Otherwise, ambiguities occur due to the somewhat periodic pattern. Another way to increase resolution is to decrease the scale factor between the physical size of a particle and the image size occupied by the particle. However, $3mm/12pixels$ was the minimum scale factor with the lenses we had at the time the images were taken and available distance between the camera and particles in our experiment setup.

In order to test the resolution improvement with sample rate decreased, the pair of images in Fig. 2-5 are used. The image on the left hand side in Fig. 2-5 is the same as one on the left hand side in Fig. 2-1, whereas the image on the right hand side in Fig. 2-5 is the second successive image. The sampling rate is decreased by half effectively (500 frames/ sec). The result is presented in Fig. 2-6 with the same correlation threshold of 0.75 as one

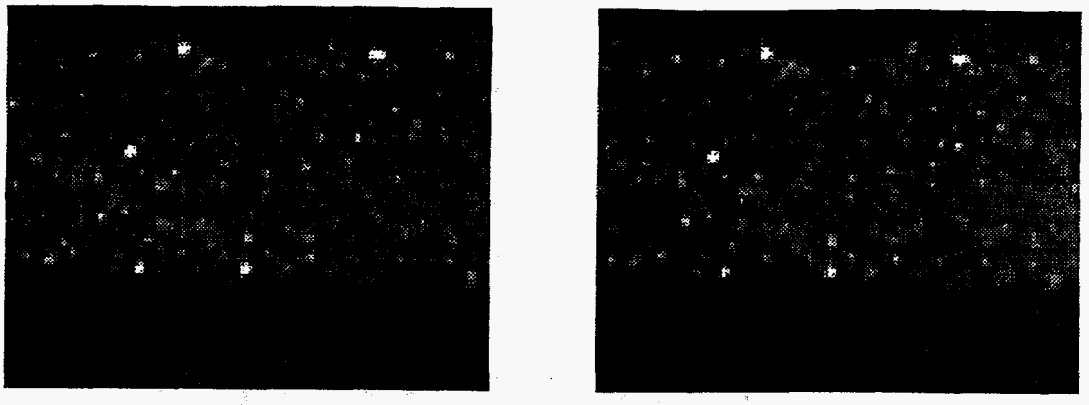

Fig. 2-1 Two successive images

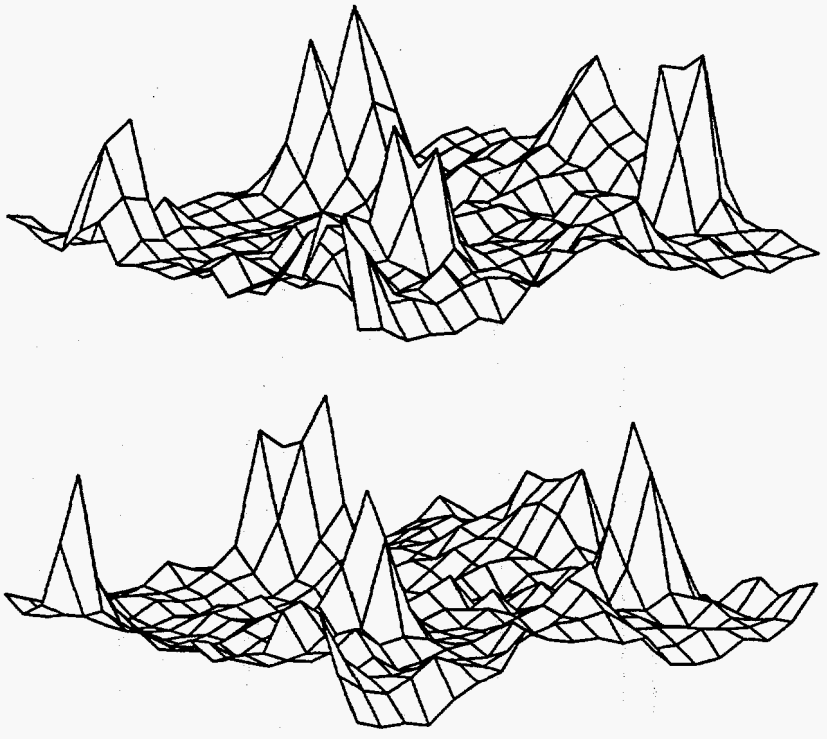

Fig. 2-2 Brightness pattern (50:69, 80:99)
top: image on the left hand side
bottom: image on the right hand side in Fig. 2-1

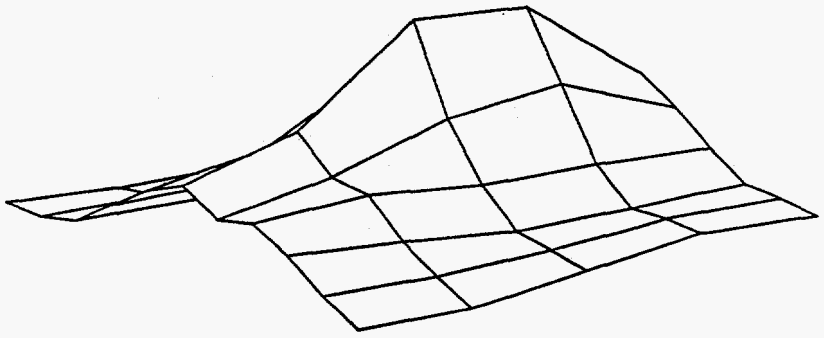

Fig. 2-3 Correlation at the center areas in Fig. 2-2

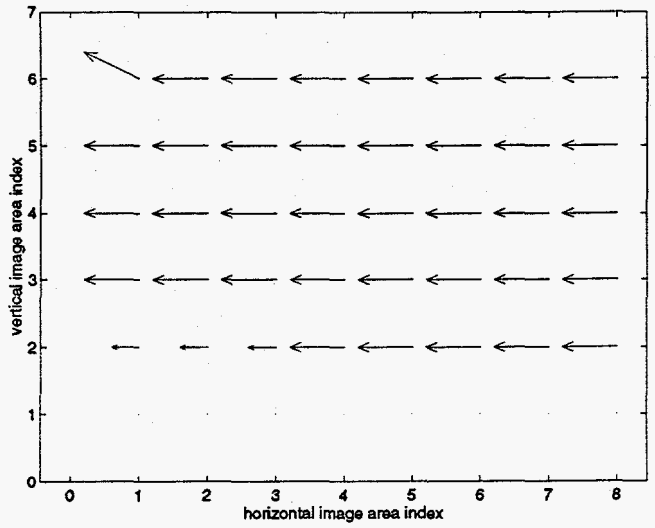

-2/ 1	-2/ 0	-2/ 0	-2/ 0	-2/ 0	-2/ 0	-2/ 0	-2/ 0
-2/ 0	-2/ 0	-2/ 0	-2/ 0	-2/ 0	-2/ 0	-2/ 0	-2/ 0
-2/ 0	-2/ 0	-2/ 0	-2/ 0	-2/ 0	-2/ 0	-2/ 0	-2/ 0
-2/ 0	-2/ 0	-2/ 0	-2/ 0	-2/ 0	-2/ 0	-2/ 0	-2/ 0
-1/ 0	-1/ 0	-1/ 0	-2/ 0	-2/ 0	-2/ 0	-2/ 0	-2/ 0
0/ 0	0/ 0	0/ 0	0/ 0	0/ 0	0/ 0	0/ 0	0/ 0

horizontal/ vertical displacement (pixels)

Fig. 2-4 Displacement field and values

in the previous result for comparison. The resolution has been improved twice to 12.5 cm/ sec, which is obvious by comparison of displacement values with those of the previous result. However, it turns out that the correlation has been reduced between two frames with the sampling rate decreased. The blanks in the displacement values correspond to lower correlation values than the threshold due to the abrupt changes of brightness pattern.

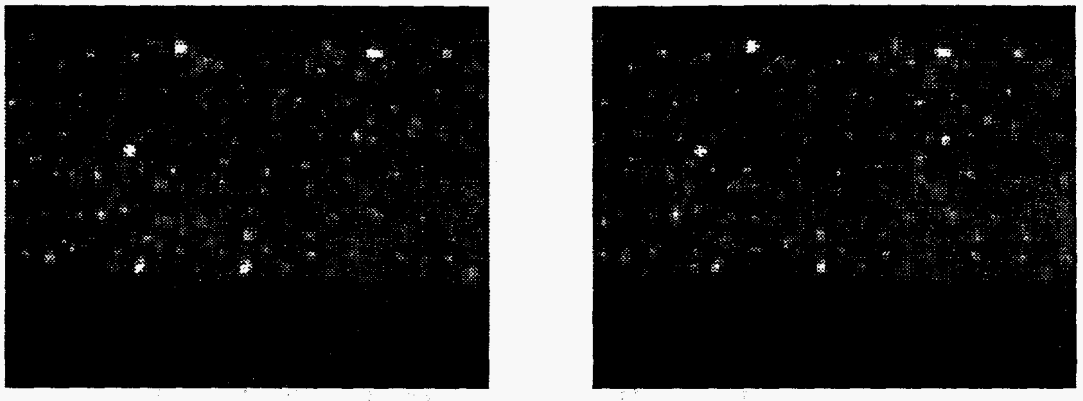

Fig. 2-5 Two successive images

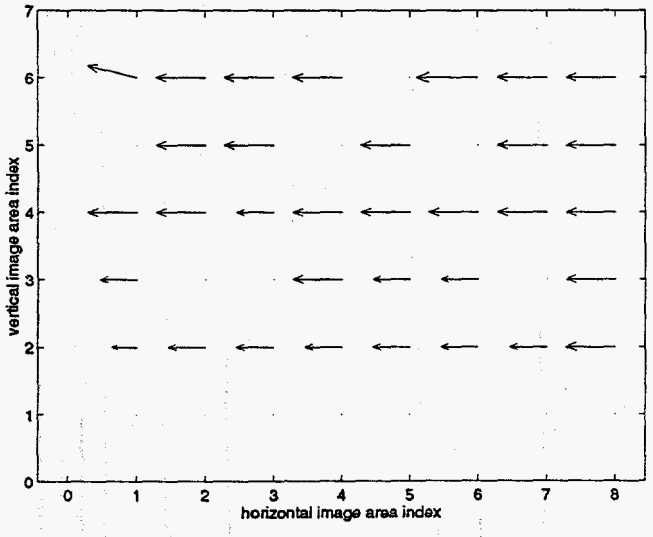

Fig. 2-6 Displacement field and values

-4/ 1	-4/ 0	-4/ 0	-4/ 0		-5/ 0	-4/ 0	-4/ 0
	-4/ 0	-4/ 0		-4/ 0		-4/ 0	-4/ 0
-4/ 0	-4/ 0	-3/ 0	-4/ 0	-4/ 0	-4/ 0	-4/ 0	-4/ 0
-3/ 0			-4/ 0	-3/ 0	-3/ 0		-4/ 0
-2/ 0	-3/ 0	-3/ 0	-3/ 0	-3/ 0	-3/ 0	-3/ 0	-4/ 0
0/ 0	0/ 0	0/ 0	0/ 0	0/ 0	0/ 0	0/ 0	0/ 0

horizontal/ vertical displacement (pixels)

Fig. 2-6 -- continued

The resolution of displacement measurement with correlation is limited by pixel spacing and the size of a window. Since equally spaced sampled data are used to get the correlation between two successive frames, the resolution is limited by pixel spacing. However, real displacement can take any value between neighboring pixels. The measurement can be made closer to the real displacement by subpixel resolution that is provided by interpolation in the correlation plane. Beyer showed that an estimate accuracy of 1/10 pixel can be obtained with correlation techniques using a practical mask size of 7 by 7 under a 30 dB signal-to-noise ratio (Musmann et al. 1985). Since the mask size for our analysis is 13 by 13, we expect to obtain at least the 1/10 pixel resolution with the interpolation. Polynomial interpolation by 10 is applied to 3 by 3 points around maximum correlation value. After applying the interpolation, a maximum value is searched in the interpolated plane to find the subpixel resolution displacement. Fig. 2-7 shows the displacement field with the interpolation for the images as shown in Fig. 2-1. The same correlation threshold of 0.75 is used. It seems that the displacements in Fig. 2-4 are rounded off

values of the interpolated displacements due to the resolution limited by pixel spacing. With the interpolation, velocity measurement resolution is improved by a factor of 10. The resolution improvement of velocity measurements allows the displacement field in Fig. 2-7 to show a displacement gradient along the height of the flow, which is expected behavior.

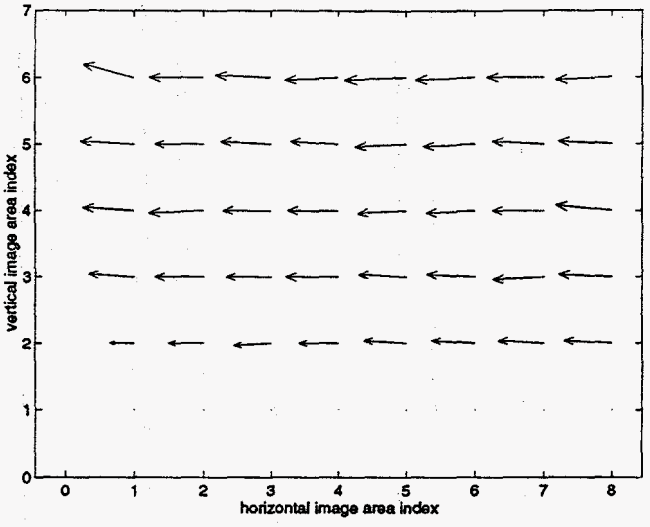

-1.9/ .5	-2.0/ 0.	-2.1/ .1	-2.0/ -.1	-2.3/ -.1	-2.2/ -.1	-2.1/ 0.	-2.1/ -.1
-2.0/ .1	-1.8/ 0.	-1.9/ .1	-1.8/ .1	-1.9/ -.1	-1.9/ -.1	-1.9/ .1	-2.0/ .1
-1.9/ .1	-2.0/ -.1	-1.8/ 0.	-1.9/ 0.	-1.8/ -.1	-1.8/ -.1	-1.9/ 0.	-2.1/ .2
-1.7/ .1	-1.8/ 0.	-1.7/ 0.	-2.0/ 0.	-1.8/ .1	-1.8/ .1	-1.9/ -.1	-2.0/ .1
-0.9/ 0.	-1.3/ 0.	-1.4/ -.1	-1.5/ 0.	-1.6 /.1	-1.6/ .1	-1.7/ .1	-1.8/ .1
0./ 0.	0./ 0.	0./ 0.	0./ 0.	0./ 0.	0./ 0.	0./ 0.	0./ 0.

horizontal/ vertical displacement (pixels)

Fig. 2-7 Displacement field and values

Validations of the Correlation for Velocity Measurement

Correlation for velocity measurement is validated in three different ways. Firstly, correlation is tested with an artificial image pair, in which displacement between the pair can be adjusted arbitrarily. Secondly, velocity measurements with correlation are compared with manual measurements for the same image pair. Lastly, averaged velocity profile along height of flow is compared with that using an optic probe.

Validation of the Correlation with an Artificial Image

The first validation is performed with an artificial image generated by a 2-D Gaussian function with standard deviation of 2.0 to simulate the brightness pattern of a particle in images. As the pattern is displaced at subpixel resolution, the results of correlation with and without the interpolation are monitored. Either of the horizontal or vertical displacements are fixed at 1.5 pixels, and the other displacements are changed from 2.0 to 2.7 in 0.1 pixel increment to evaluate the result for the horizontal and vertical displacement separately. The result is summarized in the following table.

Table 2-1 Comparison between the correlation with and without the interpolation

Real displacement		Correlation without interpolation		Correlation with interpolation	
horizontal	vertical	horizontal	vertical	horizontal	vertical
1.5	2.0	1	2	1.5	2.0
1.5	2.1	1	2	1.5	2.1
1.5	2.2	1	2	1.5	2.2
1.5	2.3	1	2	1.5	2.3
1.5	2.4	1	2	1.5	2.4

Table 2-1 -- continued

Real displacement		Correlation without interpolation		Correlation with interpolation	
horizontal	vertical	horizontal	vertical	horizontal	vertical
1.5	2.5	1	2	1.5	2.5
1.5	2.6	1	3	1.5	2.6
1.5	2.7	1	3	1.5	2.7
2.0	1.5	2	1	2.0	1.5
2.1	1.5	2	1	2.1	1.5
2.2	1.5	2	1	2.2	1.5
2.3	1.5	2	1	2.3	1.5
2.4	1.5	2	1	2.4	1.5
2.5	1.5	2	1	2.5	1.5
2.6	1.5	3	1	2.6	1.5
2.7	1.5	3	1	2.7	1.5

It turns out that the result of the correlation without the interpolation is a rounded off version of the real displacement, and the correlation with the interpolation produces perfect solution with the artificial image. Also, this result demonstrates that the estimate accuracy of 1/10 pixel can be obtained with the interpolation.

Comparison of the Correlation with Manual Displacement Measurement

As another way to validate the correlation for velocity measurement, the velocity measurements with correlation are compared with manual displacement measurement for the same image set as shown in Fig. 2-8, in which the top image precedes the bottom image by a sampling time of 1 msec. Locations of 32 recognizable glass particles in both images are measured manually and the correlation outputs from masks (without the inter-

polation), which each particle overlaps, are compared in the following table. Locations are presented 'horizontal, vertical' position with respect to upper left origin of the images

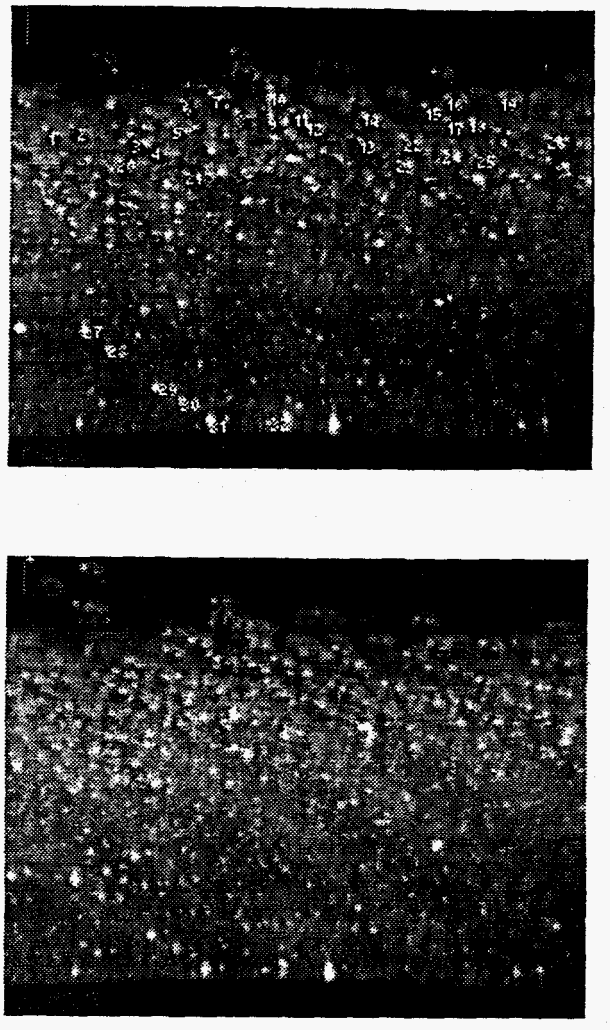

Fig. 2-8 Two successive images

The differences between the manual displacement measurement and the correlation in term of root mean square in both directions turn out to be within one pixel, which has to take into account errors involved in the manual measurement and the way the two methods are compared.

Table 2-2 Comparison of the correlation with manual displacement measurement

Part-icle No.	Location in the preced-ing image	Location in the current image	Displace-ment	Correlation	Correlation - Displacement
1	18, 52	11, 52	-7, 0	-6, 0	1, 0
2	29, 51	22, 51	-7, 0	-5, 0	2, 0
3	51, 56	45, 57	-6, 1	(-6, 0), (-6, 0)	(0, -1), (0, -1)
4	61, 59	55, 59	-6, 0	(-6, 0), (-5, 0)	(0, 0), (1, 0)
5	70, 50	64, 50	-6, 0	-6, 0	0, 0
6	73, 41	68, 40	-5, -1	(-6, 0), (-5, 0)	(-1, 1), (0, 1)
7	85, 37	79, 36	-6, -1	-5, 1	1, 2
8	96, 45	90, 44	-6, -1	-6, 1	0, 2
9	109, 47	103, 47	-6, 0	-6, 0	0, 0
10	110, 37	104, 36	-6, -1	-5, 0	1, 1
11	119, 44	113, 44	-6, 0	(-6, 0), (-5, 0), (-5, -1), (-5, 0)	(0, 0), (1, 0), (1, -1), (1, 0)
12	125, 49	121, 48	-4, -1	-5, 0	-1, 1
13	146, 57	142, 57	-4, 0	(-5, 0), (-5, 0)	(-1, 0), (-1, 0)
14	148, 45	143, 45	-5, 0	-5, 0	0, 0
15	174, 40	168, 40	-6, 0	(-6, 0), (-5, 0)	(0, 0), (1, 0)
16	183, 37	177, 37	-6, 0	(-5, 0), (-5, 1)	(1, 0), (1, 1)
17	181, 47	176, 47	-5, 0	(-6, 0), (-6, 0)	(-1, 0), (-1, 0)
18	193, 48	187, 48	-6, 0	-6, 0	0, 0
19	206, 37	200, 38	-6, 1	-6, 0	0, -1
20	47, 65	42, 65	-5, 0	(-6, 0), (-4, 0)	(-1, 0), (1, 0)
21	74, 70	70, 70	-4, 0	(-6, 2), (-4, 0)	(-2, 2), (0, 0)
22	164, 53	158, 54	-6, 1	(-5, 0), (-5, 0)	(1, -1), (1, -1)
23	162, 66	156, 65	-6, -1	(-5, 0), (-5, -1)	(1, 1), (1, 0)
24	181, 61	177, 61	-4, 0	(-5, 0), (-5, 0)	(-1, 0), (-1, 0)
25	195, 61	188, 62	-7, 1	(-5, 0), (-5, 0)	(2, -1), (2, -1)

Table 2-2 -- continued

Particle No.	Location in the preceding image	Location in the current image	Displacement	Correlation	Correlation - Displacement
26	224, 54	218, 53	-6, -1	(-6, 0), (-6, 0), (-6, 0), (-6, -1)	(0, 1), (0, 1), (0, 1), (0, 0)
27	33, 133	32, 133	-1, 0	-2, -1	-1, -1
28	44, 141	44, 141	0, 0	(-1, 0), (0, 0)	(-1, 0), (0, 0)
29	63, 158	63, 158	0, 0	0, 0	0, 0
30	76, 163	75, 164	-1, 1	0, 0	1, -1
31	86, 172	86, 171	0, -1	0, 0	0, 1
32	111, 171	112, 171	1, 0	0, 0	-1, 0

RMS
0.92, 0.78

Comparison of the Correlation with Measurement using Optical Probes

The average velocity profile using correlation is compared with that using an optic probe. The optic probe is a conventional granular flow velocity measuring device which consists of a pair of optic sensors separated by the distance on the order of the particle size. The optic probe is installed in the same plane, generally parallel to particles primary flow direction. Each sensor has optic transmitter and receiver. As a particle travels along the line connecting two sensors, the particle is detected by both sensors. The signal from one sensor is shifted in time with respect to that from the other sensor. Thus, the velocity of a particle can be measured by estimating the time delay between two sensors.

We make a comparison of velocity measurements obtained under the following conditions: chute width, 15 cm; angle, 23 degree; entrance gate height, 5 cm; and bumpy

base. These conditions produce very steady flow. The bumpy base refers to one type of chute base used in our experiments. 3 mm glass particles are epoxied to perforated aluminum plate in a densely packed hexagonal pattern as shown in Fig. 2-9. The reference of flow height is upper surface of smooth aluminum base plate.

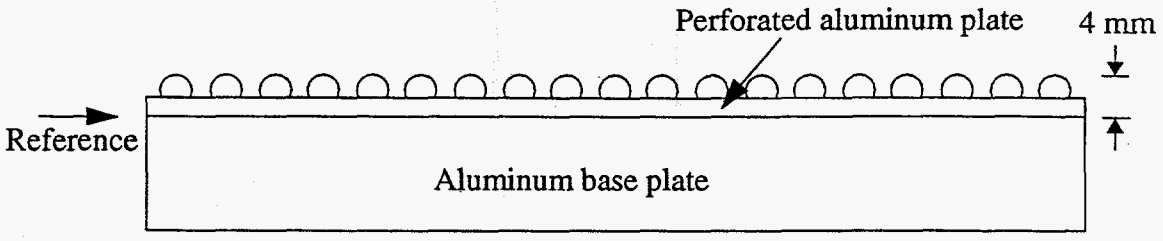

Fig. 2-9 Bumpy base and reference of flow height

The comparison is presented in Fig. 2-10, in which measurements using correlation (circles) and measurements using optic probe (crosses) are compared. The images are taken with record rate of 1000 frames/ sec, among which 8 pairs of images with 0.1 sec separated between the pairs are used for the velocity measurement (total elapse time: 0.7 sec). Correlation with the interpolation is taken for each pair of the images, then the horizontal velocity measurements for 8 pairs are averaged to produce the velocity profile.

Optic probe data are taken for 1 minute with a sampling rate of 20, 000 samples/ sec per measuring height (1, 200, 000 samples). Then, the data are divided into 240 sections (5, 000 samples/ section), and the velocity is measured for every section using the variance normalized correlation. Average of measurements over 240 sections are taken.

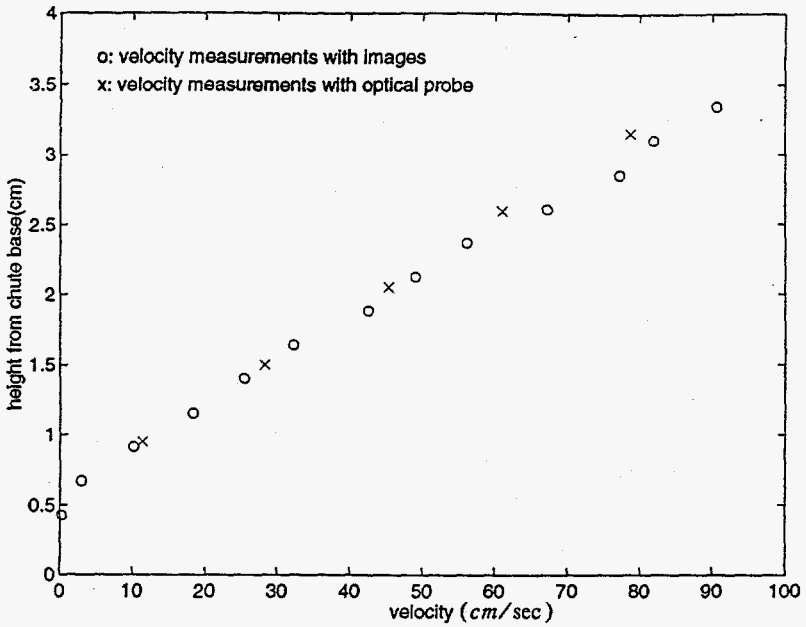

Fig. 2-10 Comparison of measurements using images and optic probe

The two methods are consistent with each other, particularly considering that two data sets were not taken at the same time. From the comparison, we have found that the image based method has some clear advantages over the optic probes. The image method can obtain synoptic measurements at many positions whereas the optic probes only measure at one location. The image method produces instantaneous velocity measurement as well as averaged velocity measurement whereas optic probes produce only averaged velocity measurement.

CHAPTER 3
VELOCITY MEASUREMENT OF FLOWING ACRYLIC PARTICLES

We presented variance normalized correlation for the velocity measurement of glass particles in the previous chapter, which is strictly an average process. It is analogous to evenly positioned matched filters from which averaged velocity measurements within each image mask are derived.

Another way to measure velocity of granular flow is to find particle locations and to determine the particle correspondence between successive frames. It is expected that errors may occur in finding the locations and the correspondence of particles across frames. However, the method will provide velocity measurements for individual particles between frames and tracking of particles in space at the same time. Accordingly, it is fundamentally a more powerful measurement technique than correlation techniques (block matching). As mentioned earlier, it is easier to obtain high quality images and to recognize individual acrylic particles than glass particles. So, acrylic particles are used to develop this method. In order to locate particles in images, several techniques are compared: synthetic discriminant function (SDF), minimum average correlation energy (MACE) filter, modified minimum average correlation energy (MMACE) filter and variance normalized correlation. Then, points representing the locations of particles are generated using a clustering technique. Finally, a Hopfield network is employed to solve the correspondence between two successive point patterns.

Locating Particles in Images

Synthetic Discriminant Function

It is well known that correlation with a matched spatial filter (MSF) is an optimal pattern recognition technique in the presence of white Gaussian noise. Objects of interest are searched with a template in the MSF. Thus, poor performance can be expected with the MSF for geometrical distortions of the input from the template. The synthetic discriminant function (SDF) was proposed to cope with the problem associated with the distortions (Casasent 1984).

The SDF is synthesized with N training image set. These N images are chosen such that they represent different distorted versions of the objects. Given the image set $\{x_n(n_1, n_2)\}$ of different distorted images of one object $x(n_1, n_2)$, the filter function $h(n_1, n_2)$ which produces a constant correlation output between $h(n_1, n_2)$ and all images $\{x_n(n_1, n_2)\}$ is appropriate for the recognition of any distorted version of object using a single filter function, i.e.,

$$x_n(n_1, n_2) \otimes h(n_1, n_2) = 1 \tag{3.1}$$

where unity is chosen arbitrarily for the constant.

Each training image is represented as a linear combination of a basis function set $\phi_m(n_1, n_2)$, i.e.,

$$x_n(n_1, n_2) = \sum_m a_{nm}\phi_m(n_1, n_2) \tag{3.2}$$

The desired SDF is represented as another linear combination of the same basis function set, i.e.,

$$h(n_1, n_2) = \sum_m b_m \phi_m(n_1, n_2). \tag{3.3}$$

By substituting equation (3.2) and (3.3) into the equation (3.1) and assuming an orthonormal set of basis functions, equation (3.1) becomes

$$x_n(n_1, n_2) \otimes h(n_1, n_2) = \boldsymbol{x}_n \cdot \boldsymbol{h} = \sum_m a_{nm} b_m = 1 \tag{3.4}$$

where the vectors $\boldsymbol{x}_n$ and $\boldsymbol{h}$ are obtained by concatenating rows or columns of the image (both are concatenated in the same manner, i.e., rowwise or columnwise) and $\boldsymbol{x}_n \cdot \boldsymbol{h}$ is the vector inner product. From equation (3.2), the basis function set $\phi_m(n_1, n_2)$ can be written as a linear combination of the training set of images $x_n(n_1, n_2)$ as

$$\phi_m(n_1, n_2) = \sum_n d_{mn} x_n(n_1, n_2). \tag{3.5}$$

Substituting equation (3.5) into equation (3.3), we obtain

$$
\begin{aligned}
h(n_1, n_2) &= b_1 \sum_n d_{1n} x_n(n_1, n_2) + b_2 \sum_n d_{2n} x_n(n_1, n_2) \\
&\quad + \cdots + b_m \sum_n d_{mn} x_n(n_1, n_2) \\
&= e_1 x_1(n_1, n_2) + e_2 x_2(n_1, n_2) \\
&\quad + \cdots + e_n x_n(n_1, n_2) \\
&= \sum_m e_m x_m(n_1, n_2) .
\end{aligned} \tag{3.6}
$$

In the equation (3.6), all coefficients of x_n are grouped into e_n. The $h(n_1, n_2)$ are written as a linear sum of input training set of image $\{x_n(n_1, n_2)\}$.

In order to determine e_n in equation (3.6) while satisfying the SDF condition of equation (3.4), equation (3.6) is substituted into equation (3.4).

$$
x_n \cdot h = x_n \cdot \left[\sum_m e_m x_m \right] = \sum_m e_m (x_n \cdot x_m) = \sum_m e_m r_{nm} = 1 \tag{3.7}
$$

Equation (3.7) can be written in matrix-vector form as

$$
\boldsymbol{Re} = \boldsymbol{u} \tag{3.8}
$$

where $\boldsymbol{u}$ denotes the vector whose element is the desired filter output for the corresponding training image and the elements of the vector $\boldsymbol{e}$ are the e_m in equation (3.8). The solution for the SDF $h(n_1, n_2)$ is thus given by deriving $\boldsymbol{e}$ from equation (3.8), i.e.,

$$e = R^{-1}u. \tag{3.9}$$

Substituting equation (3.9) into the equation (3.6), we finally obtain the SDF solution,

$$h = xR^{-1}u \tag{3.10}$$

where matrix x, whose column is x_i, is defined as

$$x = [x_1, x_2, \ldots, x_N] \tag{3.11}$$

N is the number of training images.Thus, synthesis of an SDF involves forming the correlation matrix of the training set of images, inverting it, and multiplying the resultant matrix by the appropriate vector u. The synthesis and test of SDF is described in Fig. 3-1

Equation (3.10) can be represented in frequency domain, i.e.,

$$H = X(X^{+}X)^{-1}u \tag{3.12}$$

where the matrix X, whose column is X_i derived from the DFT of the image x_i, is defined as

$$X = [X_1, X_2, \ldots, X_N] \tag{3.13}$$

The superscript + denotes the conjugate transpose of a complex matrix. Equation (3.12) is derived using the linearity property and the fact that correlation at zero lag corresponds to the sum of products of Fourier transforms of the signals being correlated.

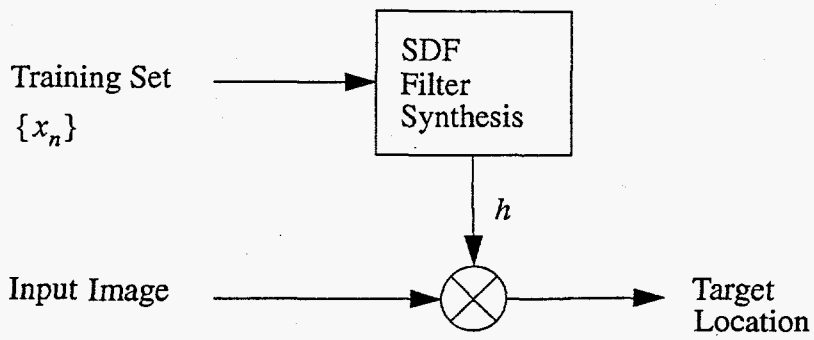

Fig. 3-1 Block diagram of SDF

Minimum Average Correlation Energy Filter

The SDF was developed to recognize geometrically distorted versions of images. However, it controls the filter output only or in the vicinity of the peak by presenting shifted versions of each training set image. For the MSF, the output of the correlator is the autocorrelation with a true target. The peaks of the autocorrelation locate true targets. However, the linear combination of correlation filters as in the SDF lacks a sharp correlation peak.

The minimum average correlation energy filter (MACE) was developed to produce sharp correlation peaks while allowing constraint on the correlation peak values, which makes easy detection of true targets in the full correlation plane (Mahalanobis et al. 1987). The ith training image is described as a 1-D discrete sequence obtained by concatenating

rows or columns of the image as in SDF. Thus, the discrete image sequence is described as a column vector x_i of dimensionality d equal to number of pixels in the image $x_i(n)$, i.e.,

$$x_i = [x_i(1), x_i(2), \ldots, x_i(d)]^T \tag{3.14}$$

The column vector X_i is derived from the DFT of the image x_i. The matrix X,whose column is X_i, is defined in equation (3.13).

The correlation $g_i(n)$ between the ith image sequence $x_i(n)$ and the filter sequence $h(n)$ is

$$g_i(n) = x_i(n) \otimes h(n). \tag{3.15}$$

The energy of the ith correlation plane is

$$\begin{aligned} E_i &= \sum_{n=1}^{d} |g_i(n)|^2 = (1/d) \sum_{k=1}^{d} |G_i(k)|^2 \\ &= (1/d) \sum_{k=1}^{d} |H(k)|^2 |X_i(k)|^2 \end{aligned} \tag{3.16}$$

The energy function is described in terms of frequency representation using Parseval's theorem. Equation (3.16) can be written using the matrix-vector form

$$E_i = H^+ D_i H \tag{3.17}$$

where the superscript + denotes the conjugate transpose of a complex vector, and D_i is a diagonal matrix of size $d \times d$ whose diagonal elements are the magnitude square of the associated element of X_i, i.e.,

$$D_i(k) = |X_i(k)|^2 \tag{3.18}$$

Equation (3.18) shows that D_i is power spectrum of $x_i(n)$.

In order to achieve good detection, it is desirable to reduce correlation output levels at the entire correlation plane except at the origin, where the imposed constraint on the peak value must be met. This is equivalent to minimizing the energy of the correlation function while satisfying constraints. In vector form, the constraint value at the origin of training image is

$$g_i(0) = \boldsymbol{X}_i^{+}\boldsymbol{H} = u_i \tag{3.19}$$

for all $i = 1, 2, \ldots, N$, where u_i is the constraint values and is also the ith element of the constraint vector $\boldsymbol{u}$. Thus in matrix-vector form, the problem is to find the frequency domain vector $\boldsymbol{H}$ that minimize $E_i = \boldsymbol{H}^{+} D_i \boldsymbol{H}$ for all i, while satisfying the constraints in equation (3.19), which is written for all training images as

$$X^{+}\boldsymbol{H} = \boldsymbol{u} \tag{3.20}$$

The solution to this problem does not exist because the simultaneous constrained minimization of all E_i ($i = 1, 2, \ldots, N$) is not possible. Instead, minimizing the average value of E_i while meeting the constraints is attempted as the name of filter (MACE) implies.

The average correlation plane energy is

$$E_{av} = (1/N) \sum_{i=1}^{N} E_i = (1/N) \sum_{i=1}^{N} \boldsymbol{H}^{+} D_i \boldsymbol{H}$$
$$= (1/N) \boldsymbol{H}^{+} \left(\sum_{i=1}^{N} D_i \right) \boldsymbol{H} \tag{3.21}$$

D is defined as

$$D = \sum_{i=1}^{N} \alpha_i D_i \tag{3.22}$$

where α_i is a constant. If all $\alpha_i = 1$, equation (3.21) can be written as

$$E_{av} = (1/N) \boldsymbol{H}^{+} D \boldsymbol{H} \tag{3.23}$$

The solution to the minimization of $\boldsymbol{H}^{+} D \boldsymbol{H}$ subject to the constraints $X^{+} \boldsymbol{H} = \boldsymbol{u}$ can be found using the method of Lagrange multipliers.

$$\boldsymbol{H} = D^{-1} X (X^{+} D^{-1} X)^{-1} \boldsymbol{u} \tag{3.24}$$

The closed form of the MACE filter is derived. Now, the property of the MACE will be investigated in conjunction with the SDF.

Let $D^{-0.5} = P$, i.e., P is a diagonal matrix whose diagonal element is the reciprocal square roots of the diagonal elements of D. Then,

$$\boldsymbol{H} = P\,(PX)\,(X^{+}PPX)^{-1}\boldsymbol{u}. \tag{3.25}$$

Let $PX = \overline{X}$, then $\boldsymbol{H}$ can be rewritten as

$$\boldsymbol{H} = P\overline{X}(\overline{X}^{+}\overline{X})^{-1}\boldsymbol{u}. \tag{3.26}$$

If we denote $\overline{X}\,(\overline{X}^{+}\overline{X})^{-1}\boldsymbol{u}$ as $\overline{\boldsymbol{H}}$, $\boldsymbol{H}$ becomes

$$\boldsymbol{H} = P\overline{\boldsymbol{H}}. \tag{3.27}$$

The vector $\overline{\boldsymbol{H}}$ is the SDF based on the transformed data $\overline{X}$. Thus, the frequency response $\boldsymbol{H}$ can be interpreted as the cascade of the matrix P (spectrum whitening filter) and SDF (based on transformed data $\overline{X}$). Equation (3.27) can be described by the block diagram in Fig. 3-2.

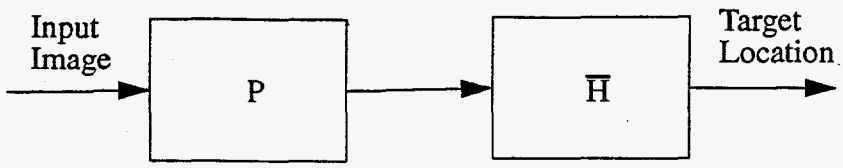

Fig. 3-2 Block diagram of MACE filter

Modification to the MACE filter

The MACE filter was developed to produce sharp peaks at locations of true targets while satisfying the constraints of peak values using the filter structure of the spectrum whitening filter followed by the SDF. However, the spectrum whitening filter induces poor generalization to distorted images from training set. On the other hand, the SDF shows good generalization at the expense of sharp peaks since it is a linear sum of correlation between each training image and an input image. Based on these properties, we propose a filter that compromises the sharp peak with good generalization by modifying the spectrum whitening stage of the MACE filter, i.e.,

$$P = \frac{I}{(1-\alpha) + \alpha D^{0.5}} \qquad 0 \le \alpha \le 1 \qquad (3.28)$$

where I is an identity matrix whose dimension is the same as that of P. For example, in the case of $\alpha = 0$, $P = I$, which means that no transform is taken in the spectrum whitening stage (P). As a result, the frequency response H becomes the SDF. In the other extreme case of $\alpha = 1$, $P = D^{-0.5}$ which is the same as the MACE formulation. There-

fore, we can design the filter which produces good generalization at the small expense of the sharp peak by adjusting the α value.

Locating Particles with Variance Normalized Correlation

Variance normalized correlation, used for the velocity measurement of glass particles, is also proposed to recognize acrylic particles in images. This process identifies particle locations. Variance normalized correlation is modified in order to extract the image data of a particle centered at the mask and to attenuate the image data between the boundary of the particle and that of the mask, i.e.,

$$r'(m,n) = \frac{\sum_x \sum_y [f'(x,y) - \bar{f}'][w'(x-m, y-n) - \bar{w}']}{\left[\sum_x \sum_y [f'(x,y) - \bar{f}']^2 \sum_x \sum_y [w'(x-m, y-n) - \bar{w}']^2\right]^{1/2}} \quad (3.29)$$

$$f'(x,y) = g(x,y) f(x,y)$$

$$w'(x,y) = g(x,y)\, w(x,y)$$

where $\bar{w}'$ is the average intensity of the mask, $\bar{f}'(x,y)$ is the average value of $f'(x,y)$ in the region coincident with $w'(x,y)$. The kernel $g(x,y)$ is a 2-D Gaussian function with appropriately chosen standard deviation such that it's distribution is the same order of the diameter of a particle in our images.

Experiment for Performance Comparison

The modified MACE filter (MMACE) is evaluated with two pairs of images; One pair is glass particles in free fall, and the other comprises acrylic particles flowing down the inclined chute. Fig. 3-3 shows two successive images, which are taken while particles are dropped in front of the camera. The image on the left hand side precedes the image on the right hand side. The image size is one fourth of total image (96 by 119). Particle image size is typically 20 pixels in diameter. It is noticeable that the brightness pattern of the lower particle is somewhat different from that of two upper particles, and the brightness of the background is not uniform. Two upper particles in the preceding image are used as training images of size, 21 by 21 pixels. Desired output amplitude of 1.0 is arbitrarily specified for these training images.

We have found that performance of the MMACE filter depends on the way it is implemented. Thus, we introduce three different implementations of the MMACE and will compare the performance of the MMACE with that of SDF, MACE and variance normalized correlation.

Implementation 1;

1) Take 2-D FFT of the training images with a FFT size on the order of the training images (e.g., 32 by 32 FFT for a training image size of 21 by 21 pixels).
2) Synthesize the filter in the frequency domain.
3) Take inverse FFT and truncate the filter coefficients to the size of the training image (21 by 21).
4) Calculate filter outputs for the input images.

Implementation 2;

1) Take 2-D FFT of the training images with the same FFT size as filter output (e.g., 116 by 139 FFT for an input image size of 96 by 119 pixels and the training image size of 21 by 21 pixels).

2) Synthesize the filter in the frequency domain.

3) Calculate filter outputs for the input images.

Implementation 3;

1) Take 2-D FFT of the training images with the same FFT size as the filter output (as in the implementation 2).

2) Calculate the P matrix.

3) Whiten the input images with the P matrix.

4) Synthesize the SDF in the spatial domain.

5) Calculate filter outputs for the input images.

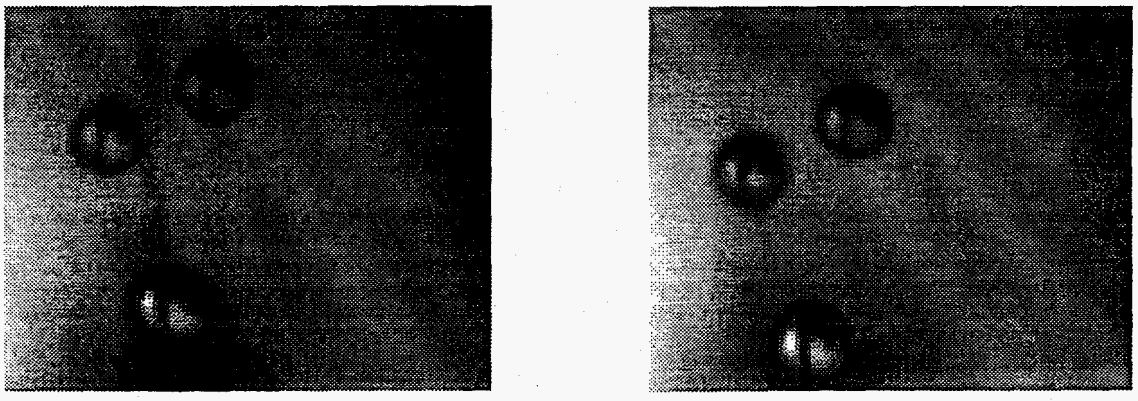

Fig 3-3 Two successive images

Now, we are going to compare the results from each implementation for the same free fall glass particle images. Fig 3-4 shows the filter outputs taken under the implementation 1 with $\alpha = 10^{-5}$. The filter output on the left side corresponds to the left image, and that on the right hand side corresponds to the right image. We will use this convention throughout this experiment. Even though the constrained peak values are met by the two top particles for the left image, the peak corresponding to the bottom particle is not distinctive, and background noise level is mostly high in all correlation plane. The filter output for the right image is even worse. These poor results are attributed to the small FFT size of the training images. The frequency contents of the training images are not well represented due to the small size of FFT. Also, some signals are discarded by taking the filter coefficient of the training image size (21 by 21 pixels) from the filter representation of size (32 by 32 pixels), which is another reason for these poor results.

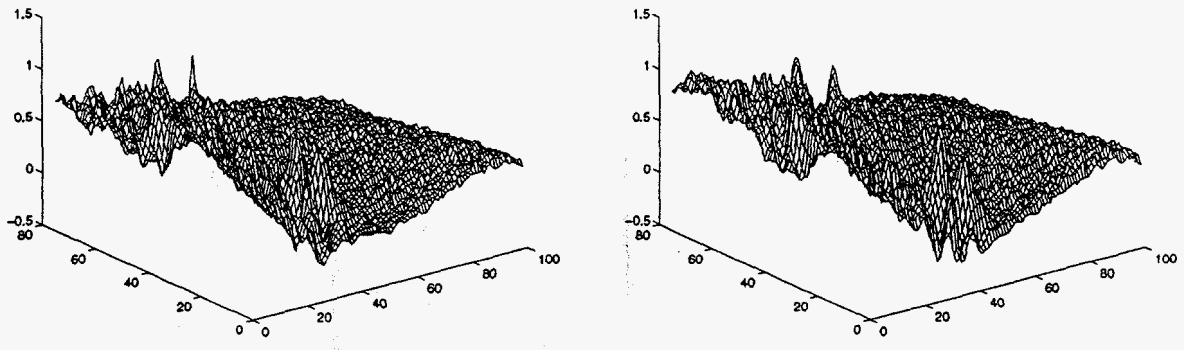

Fig. 3-4 MMACE filter output (implementation 1, $\alpha = 10^{-5}$)

Fig 3-5 shows the filter outputs taken under the implementation 2 with $\alpha = 10^{-5}$. The filter output for the left image has one peak that is smaller than the constrained value; there are no distinctive peaks at both filter outputs. However, it is obvious that the noise level in this implementation is much lower than the previous results. The discrepancy between peak values in the filter output and the constrained value is caused by the difference of frequency resolution in the FFT. That is, the training image of size 21 by 21 pixels is used for 116 by 139 FFT in the synthesis whereas the input image of size 96 by 119 pixels is used for the same size FFT in the test (The FFTs are taken with zero padding in both the synthesis and the test).

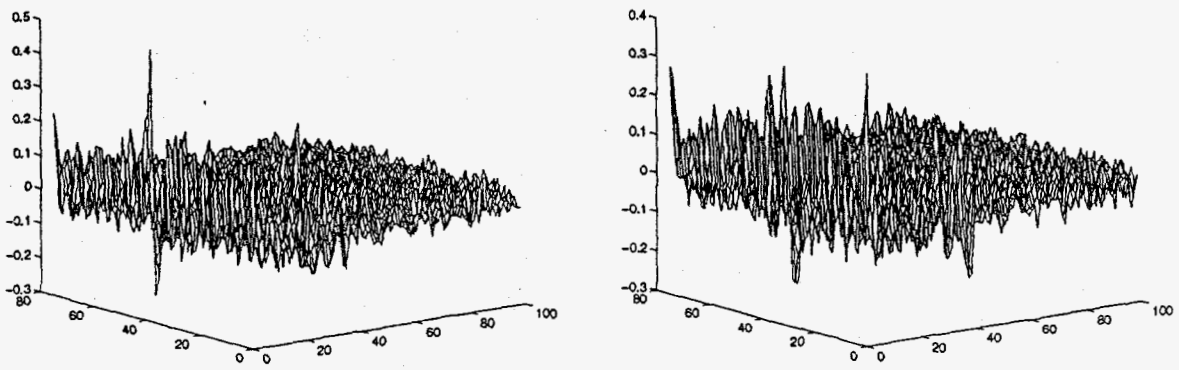

Fig. 3-5 MMACE filter output (implementation 2, $\alpha = 10^{-5}$)

In order to cope with the problem associated with the frequency resolution, we implement the filter based on the interpretation of the MACE filter in conjunction with SDF. As discussed before, the MACE filter is equivalent to the cascade of the spectrum whitening filter and SDF based on transformed data by the spectrum whitening filter. Thus, we prewhiten the input images with the P matrix, then the SDF based on the trans-

formed data is applied (implementation 3). Since the SDF is implemented in the spatial domain, the problem associated with the frequency resolution does not exist. Fig. 3-6 shows the filter outputs taken under the implementation 3 with $\alpha = 10^{-5}$. The constrained peak value at the two top locations is met, and another peak value corresponding to the bottom particle is almost the same as the constrained value for the left image. The filter output for the right image demonstrates good generalization with this implementation.

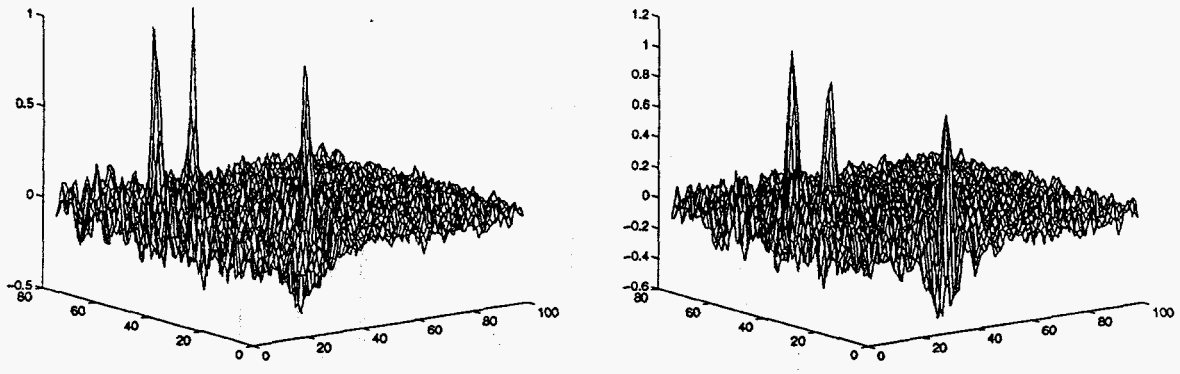

Fig. 3-6 MMACE filter output (implementation 3, $\alpha = 10^{-5}$)

Now, in order to compare performances of SDF, MACE and MMACE, we try to change α value to 0 (SDF) and to 1 (MACE). Fig. 3-7 and 3-8 show the filter outputs taken under implementation 3 with $\alpha = 0$ and $\alpha = 1$, respectively. As expected, the filter outputs with $\alpha = 0$ (SDF) show broad peaks and are dominantly affected by the bright spots inside particles rather than the particle pattern. The filter outputs with $\alpha = 1$ (MACE) show very sharp peaks (one pixel width) that meet the constrained value and higher noise level than those with $\alpha = 10^{-5}$ (MMACE). However, the other peak corre-

sponding to the bottom particle is not distinctive enough in the filter output for the left image and the filter output for the right image shows no distinctive peaks. Increasing the number of training images may produce comparable generalization to the previous result ($\alpha = 10^{-5}$).

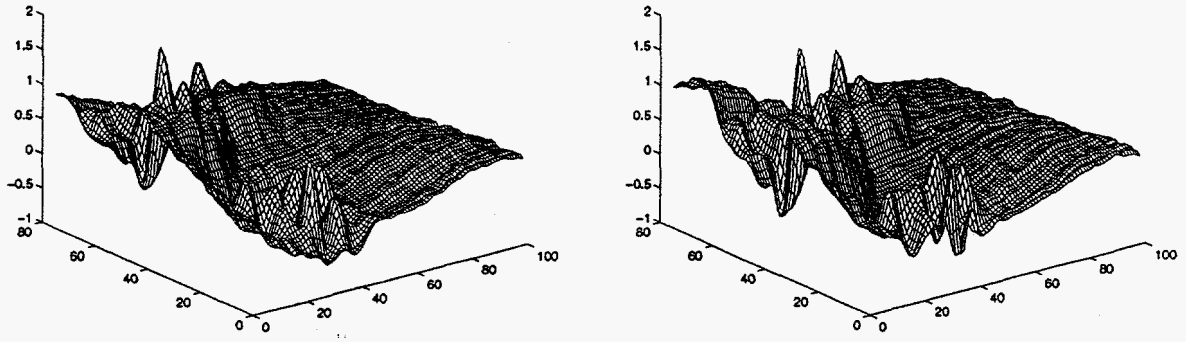

Fig. 3-7 MMACE filter output (implementation 3, $\alpha = 0$)

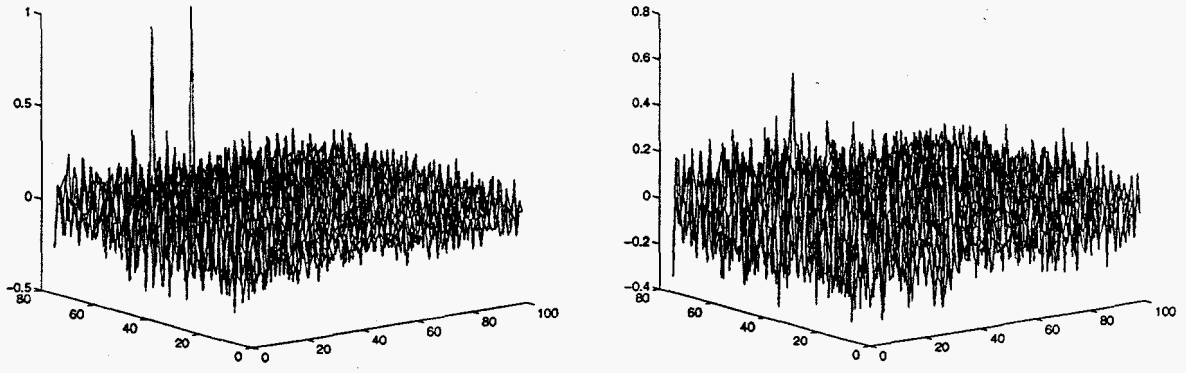

Fig. 3-8 MMACE filter output (implementation 3, $\alpha = 1$)

We have demonstrated that the performance of MACE filter is very sensitive to the implementations, and the implementation 3 produces the best performance in terms of

sharpness of peaks and generalization. Also, we compared the performance of MMACE filter with SDF and MACE filter and showed that the small value of α (10^{-5}) made a significant difference in the particle recognition performance.

We also evaluate variance normalized correlation with the same test images. The left upper particle in the left image in Fig. 3-3 is taken as a template, and a 2-D Gaussian function with the standard deviation of 4 is applied to take image data of the particle. Fig 3-9 shows the results, in which correlation is dominated by the two bright spots inside each particle and correlation values at the background are much higher than those of the MMACE filter. However, one peak is higher than the other between two peaks belonging to each particle and the peaks are distinctive enough to be discriminated against the background. By choosing an appropriate threshold, the particles can be located. Thus, these results show that variance normalized correlation is applicable to recognize objects where the brightness patterns of the objects are consistent or the distortion of input images is not considerable.

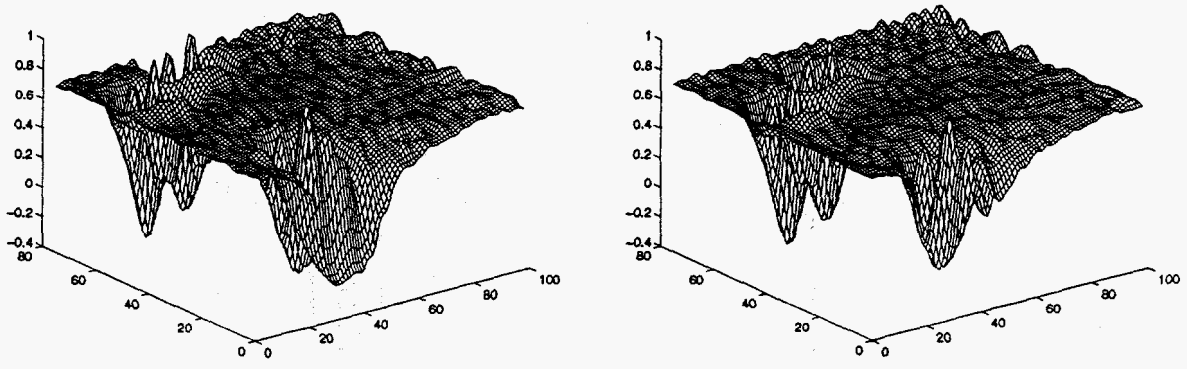

Fig. 3-9 Correlation output

Another pair of flowing acrylic particle images in Fig. 3-10 is evaluated with the MMACE filter and the variance normalized correlation. The image on the left hand side precedes the image on the right hand side by a sampling time of 1 msec. The image size is one fourth of total image (96 by 119). Nine particles in the preceding image are numbered for reference. The brighter particles like 6, 7 and 9 have white color and others have orange color, which causes brightness difference. The MMACE filter with $\alpha = 10^{-5}$ is synthesized with four particles labelled 1, 2, 3 and 9 as true-class objects and image area at upper left corner, i.e., background as false-class object. The filter output amplitudes of 1.0 and 0.0 are arbitrarily specified for the true and false-class target, respectively. The image size of these five training images is typically 13 by 13 pixels. Since most of particles are darker, three darker particles 1, 2, 3 and one brighter particle 9 are used as the true-class objects. The filter outputs are presented in Fig. 3-11. A threshold of 0.5 is used to get distinctive peaks. Every contour corresponds to the filter output greater than 0.5.

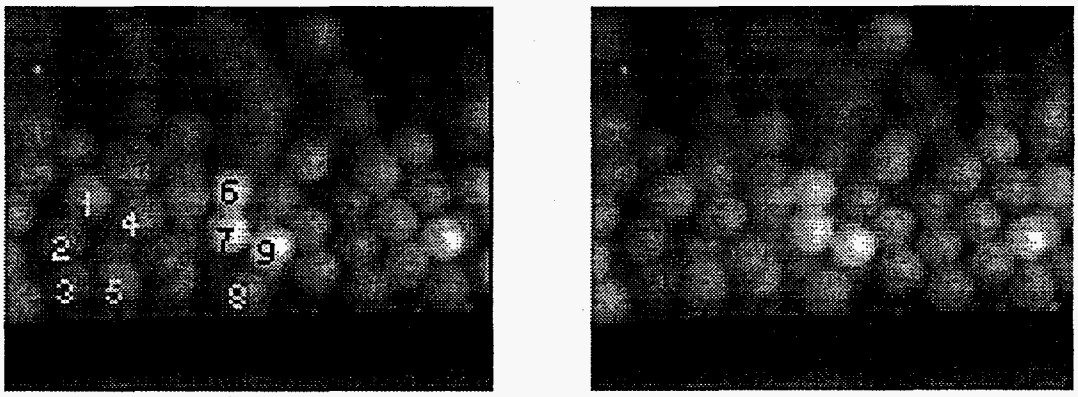

Fig. 3-10 Two successive images

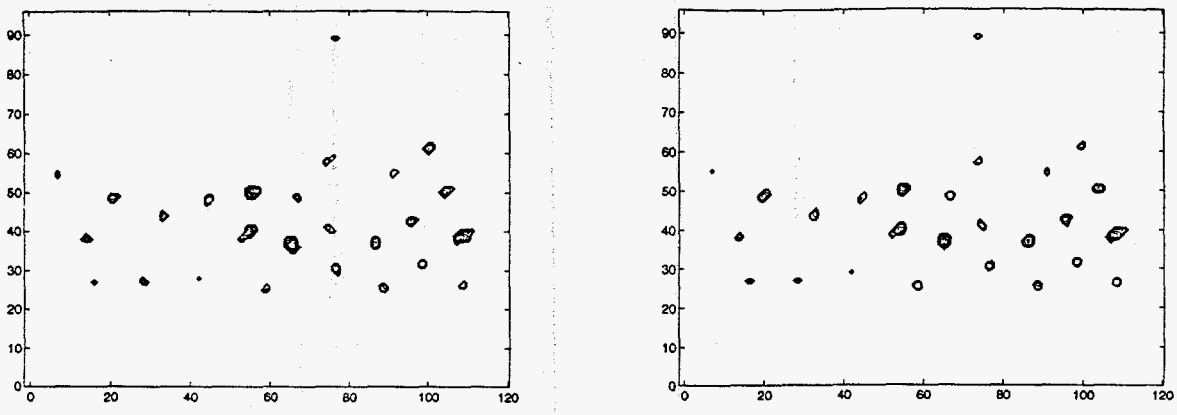

Fig. 3-11 MMACE filter output

Using a receiver operating characteristic (ROC), the detection performance of MACE filter is compared with that of MMACE filter for acrylic particle images. Also, the detection performance of each filter is evaluated with different number of training images. The MACE ($\alpha = 1$) and MMACE filter ($\alpha = 10^{-5}$) are synthesized with 2 sets of training images in Fig. 3-10. One set of training images is the same as the previous case (4 particles labelled 1, 2, 3 and 9 as true-class objects and image area at upper left corner, i.e., background as false-class object). The other set of training images includes nine particles labelled 1 through 9 and image area at upper left corner. The number of detection and false alarm is counted in the filter output for 6 test images (192 by 239) as the threshold is changed from 0.3 to 0.9 in 0.1 increment. The resultant ROC is presented in Fig. 3-12, which shows that the detection performance of MMACE filter outperforms that of MACE filter for both training image sets. The detection performance of MACE filter is improved with increased number of training images, however the detection performance of MMACE filter is a little worsened with increased number of training images.

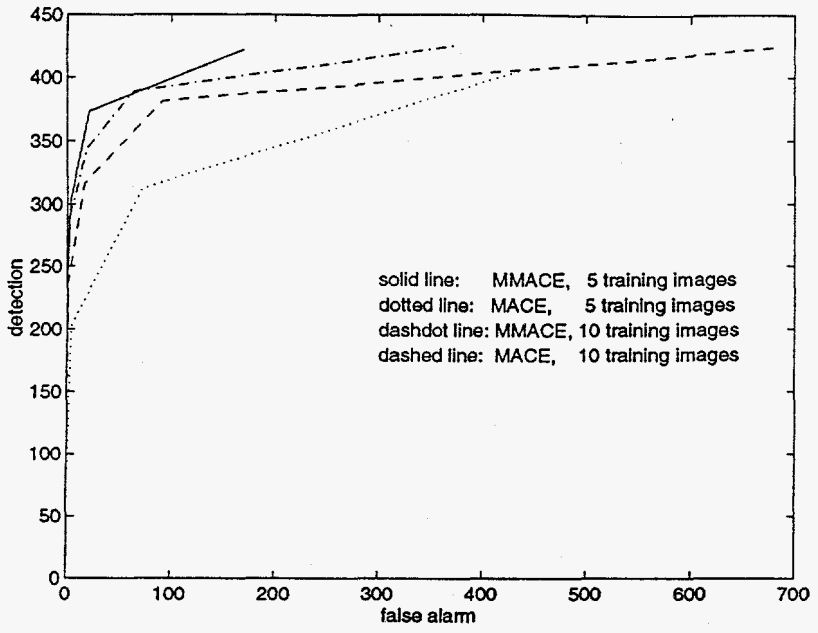

Fig. 3-12 ROC curves for MACE and MMACE filters

For the performance comparison, variance normalized correlation is applied to the two successive images in Fig. 3-13 which are the same as those in Fig. 3.10. The particle labelled 't' in the preceding image is used as a template, and a Gaussian function with a standard deviation of 2.5 is used for extraction of the image data of the particle. Fig 3-14 shows the correlation output using a threshold of 0.985. Each contour corresponds to a correlation output greater than 0.985. Since variance normalized correlation is independent of scale changes in the brightness pattern of both the template and the image area coincident with the template, it produces valid outputs for brighter particles. Fig 3-14 shows that variance normalized correlation recognizes particles that can be perceived by the human eye with just one template containing the typical brightness pattern of the particles.

In order to be comparable to variance normalized correlation, the MMACE may need to be synthesized with larger number of training images. Throughout this experiment, we have found that variance normalized correlation produces very good generation in the images that have consistent brightness patterns: since the particles have the same spherical shapes, they do not cause distortions in the images involved in rotation. The MMACE filter is expected to work fairly well in the images that have inconsistent brightness patterns such as irregularly shaped particles if the filter is synthesized with considerable number of training images.

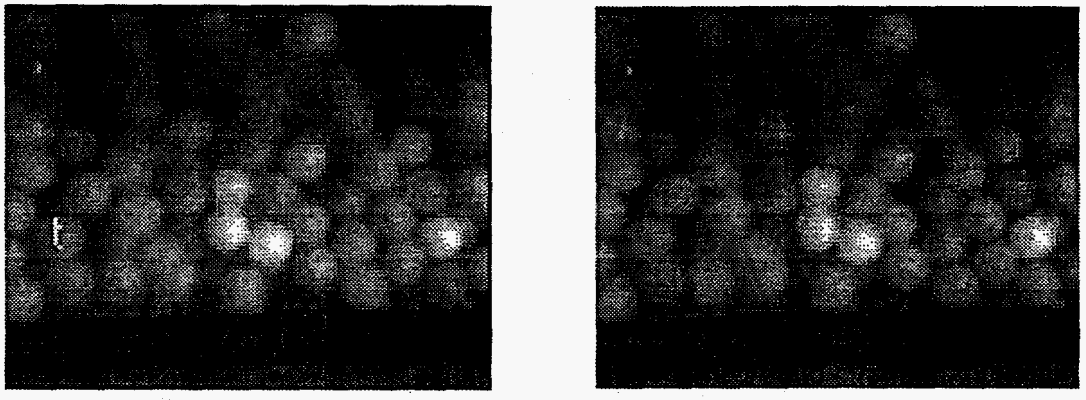

Fig. 3-13 Two successive images

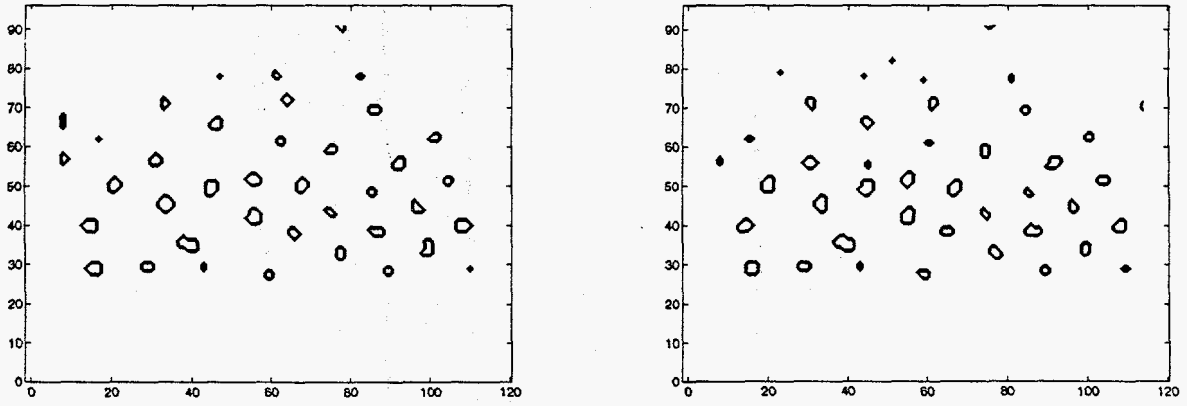

Fig. 3-14 Correlation output

Generation of Point Patterns

We are going to generate point patterns from the correlation plane, in which each point represents the location of the corresponding particle in images. Since variance normalized correlation produces good generalization in the recognition of acrylic particles, the correlation outputs as shown in Fig. 3-14 are used for generation of point patterns.

With the correlation output, a point that has maximum correlation value among the points inside each contour is searched and assigned as the location of the particle. In other words, the locations of the maximum correlation provide the coordinates of the particle centers in the image. A clustering technique (Pao 1989) is applied to group points of high correlation such that the distance between a point and its corresponding clustering center is less than a cluster distance of 5 pixels because one particle diameter is typically 12 pixels, and particles are densely packed. Then, the locations that have maximum value of correlation output in every group are searched for. Fig. 3-15 shows the resultant point patterns for the preceding image (circles) and the current image (crosses). Most of particles in one image have their correspondence in the other image, however some particles are not detected. These missed detections are caused by image edges, noise in the images and occlusions of particles. We will discuss now how to make the correspondence between two point patterns that do not have perfect correspondence.

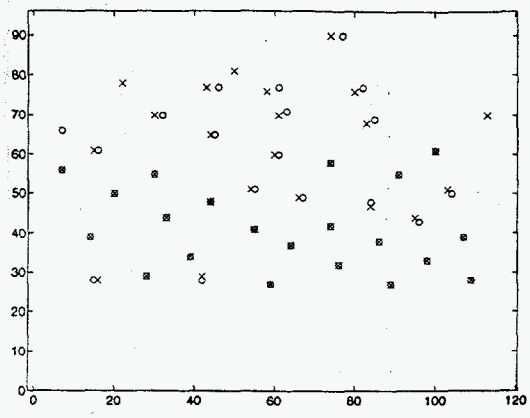

Fig. 3-15 Point patterns

Point Correspondence

There have been many approaches for solving the correspondence problem such as graph matching (Tsai and Fu 1979), or relaxation techniques (Ranade and Rosenfeld 1980; Kahl et al. 1980), in which the compatibility between matched features is measured to obtain the best solution. The problems associated with these methods are that conventional graph matching techniques are computationally complex, and the relaxation technique is inherently a local optimization method. It is sometimes difficult to determine a suitable update rule for the relaxation technique. However, a neural network can be employed for the correspondence problem by formulating it as a constrained optimization where all the constraints on the solution can explicitly be included in the cost function. Minimization of the cost function can then be achieved by a recurrent network such as the Hopfield network.

Hopfield Network

The Hopfield network is a highly parallel neural system (Hopfield 1982; Hopfield 1984; Hopfield and Tank 1985; Hopfield and Tank 1986; Bruck and Goodman 1988). Since we are dealing with a correspondence problem, processing elements are arranged in a matrix form ($M \times N$) whose elements are identified by a set of double indices x and i indicating rows and columns, respectively. The input-output relation of a processing element on row x and column i is governed by $V_{xi} = g(U_{xi})$, where g is the sigmoid function as shown in Fig. 3-16. Connection between processing elements, i.e., synapse, $T_{xi,yj}$ connects the output of processing element yj to the input of processing element xi. The network also has an externally supplied input I_{xi} to each processing element. The network, represented with lexicographic ordering the rows of the processing neurons, is shown in Fig. 3-17. The ordinary differential equation describing dynamics of the processing elements in the Hopfield network is

$$\frac{dU_{xi}}{dt} = -\frac{U_{xi}}{\tau} + \sum_{y=1}^{M}\sum_{j=1}^{N} T_{xi,yj}V_{yj} + I_{xi} \qquad (3.30)$$

$$V_{xi} = g(U_{xi}) = \frac{1}{1 + exp(-\beta U_{xi})}$$

where τ is a time constant. For an initial-value problem, all the initial values of processing elements U_{xi} at time $t = 0$ are given, and the time evolution of processing elements is described by this equation. Hopfield showed that the network with symmetric connections $(T_{xi,yj} = T_{yj,xi})$ always leads to convergence to stable states, i.e., the output of all processing elements approach constant values. Also, when the width of the transition of the

sigmoid function is narrow, i.e., the high gain limit, the stable states of a network comprised of $M \times N$ neurons, are the local minima of the energy function for the Hopfield network defined as

$$E = -\frac{1}{2}\sum_{x=1}^{M}\sum_{i=1}^{N}\sum_{y=1}^{M}\sum_{j=1}^{N} T_{xi,yj}V_{xi}V_{yj} - \sum_{x=1}^{M}\sum_{i=1}^{N} V_{xi}I_{xi} \tag{3.31}$$

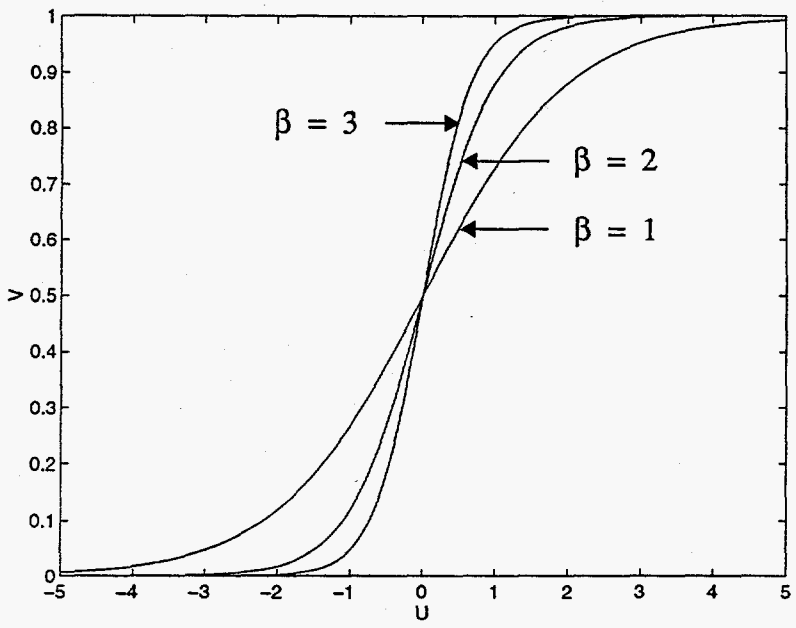

Fig. 3-16 Input-output relation of a processing element

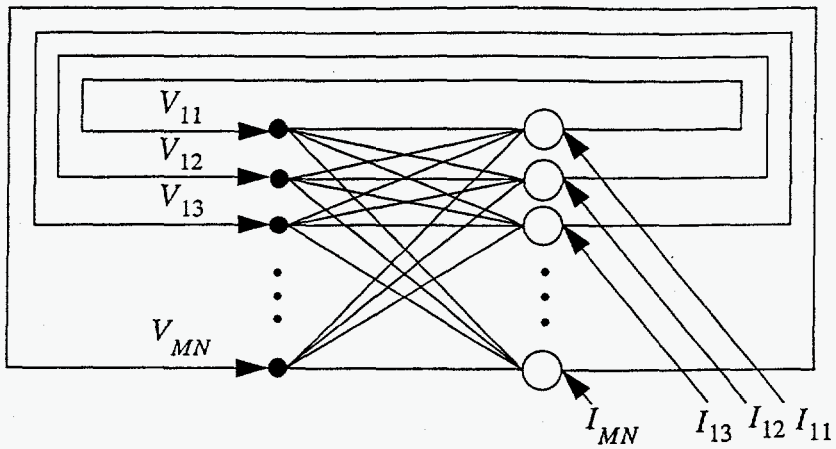

Fig. 3-17 Hopfield network

Point Correspondence using the Hopfield Network

The point correspondence problem can be formulated as a constrained optimization where the cost function (i.e., the energy function in the Hopfield network) representing the constraints on the point correspondence problem, is minimized (Barnard and Casasent 1989; Nasrabadi and Choo 1992). To solve the correspondence problem, we construct the energy function in the form of equation (3.31), whose local minima correspond to solutions for the point correspondence.

It is assumed that the 2-dimensional coordinates of points from two successive images have been obtained and denoted by $A = \{a_1, a_2, \cdots, a_N\}$, $B = \{b_1, b_2, \cdots, b_M\}$. Processing elements arranged in a matrix form converge to the stable state corresponding to the best point matching. The output states of a $M \times N$ permutation matrix V, whose rows refer to point pattern B, columns refer to point pattern A, is interpreted as

$$V_{xi} = \begin{cases} 1 & \text{if point } x \text{ in pattern } B \text{ matches point } i \text{ in pattern } A \\ 0 & \text{otherwise} \end{cases} \quad (3.32)$$

For example, for correspondence between 5 points from one image, $A = \{a_1, a_2, a_3, a_4, a_5\}$ and 4 points from the other image, $B = \{b_1, b_2, b_3, b_4\}$ using total 20 processing elements, the processing element states

	a_1	a_2	a_3	a_4	a_5
b_1	0	0	0	0	1
b_2	0	1	0	0	0
b_3	0	0	0	0	0
b_4	0	0	1	0	0

shown in the table indicate that b_1 has correspondence to a_5, b_2 to a_2, no correspondence of b_3 and b_4 to a_3. This means that there can be at most one "1" output in each row and column. If there is no correspondence for a given point in one image to the other image, the corresponding row or column will have only zero entries. Calculating all distances among points between two patterns produces a $M \times N$ distance matrix $dAB = \{dAB(x, i)\}$. Likewise, calculating all distances among points within each pattern produces a $N \times N$ distance matrix $dA = \{dA(i, j)\}$ and $M \times M$ distance matrix $dB = \{dB(x, y)\}$. Since images are taken fast enough to guarantee that the displacements are less than the diameter of a particle, the point correspondence is found under the constraint that the sum of displacements between matched points is minimized. We also

impose a rigidity constraint which requires that the distance $dA(i,j)$ between points i and j of pattern A should equals the distance $dB(x,y)$ between matched points x and y of pattern B, respectively. This constraint may seem to conflict with the motion of individual particles, however we expect that the rigidity is maintained between successive frames to some extent due to the high speed images and the flowing particle behavior. Besides, the correspondence is evaluated in local image neighborhoods that have small variation in displacements, as will be shown in the experiments. Based on the above discussion, we construct the following energy function,

$$E = \frac{A}{2}\sum_{x=1}^{M}\sum_{i=1}^{N}\sum_{j\neq i,\,j=1}^{N} V_{xi}V_{xj} + \frac{B}{2}\sum_{i=1}^{N}\sum_{x=1}^{M}\sum_{y\neq x,\,y=1}^{M} V_{xi}V_{yi}$$

$$+ \frac{C}{2}\left(\sum_{x=1}^{M}\sum_{i=1}^{N} V_{xi} - N_1\right)^2 + \frac{D}{2}\sum_{x=1}^{M}\sum_{i=1}^{N} V_{xi}dAB(x,i)$$

$$+ \frac{E}{2}\sum_{x=1}^{M}\sum_{y\neq x,\,y=1}^{M}\sum_{i=1}^{N}\sum_{j\neq i,\,j=1}^{N} V_{xi}V_{yj}|dA(i,j) - dB(x,y)| \qquad (3.33)$$

the minimum of which corresponds to the best match. The first term equals zero if and only if there is no more than one "1" at each row of V, which means that one point in pattern B is not allowed to be matched to more than one point in pattern A. The second term equals zero if and only if there is no more than one "1" at each column of V. The third term equals zero if and only if there are N_1 entries of "1" in the matrix V. The fourth term refers to the minimization of sum of displacements between corresponding points, and the fifth term refers to the rigidity constraint. Comparing equation (3.33) with (3.31), the connection matrix turns out to be

$$T_{xi,yj} = -A\delta_{xy}(1-\delta_{ij}) - B\delta_{ij}(1-\delta_{xy}) - C$$
$$-E(1-\delta_{xy})\,(1-\delta_{ij})\,|dA(i,j) - dB(x,y)| \qquad (3.34)$$

where $\delta_{ij} = 1$ if $i = j$ and 0 otherwise

The external input is

$$I_{xi} = CN_1 - DdAB(x,i) \qquad (3.35)$$

The outputs of the stable state of the above system, that corresponds to a minimum of the energy function, give the best solution for the correspondence problem.

Experiments of Point Correspondence using the Hopfield Network

Point correspondence is tested with artificial point patterns in the experiment 1 and with real point patterns in the experiment 2. In the experiment 1, grid point patterns are used to test translational and rotational motion. In the experiment 2, point patterns from a rotating bumpy base sample and flowing acrylic particles down the inclined chute are used.

Experiment 1: Point Correspondence with Grid Point Patterns

Equally spaced grid point patterns are used to test the performance of the point correspondence. These patterns may produce the most ambiguous motions in some cases if the motion is analyzed at a local area. For example, if a large rectangular grid is dis-

placed by one interpoint distance, the evaluation at the local area of the interior grid shows no motion at all. The motion can be realized by noting that points do not match up at the boundary. Therefore, the interaction among the matching points is required to have a global solution for this problem, which is provided by the interconnected processing elements of the Hopfield network. In the following experiments, we will show the performance of the point correspondence for the translational (ambiguous) and rotational motion. Also, the performance will be evaluated for the case of mainly translational motion with smaller random motion of each point and a missing point, which is closer to real patterns derived from images due to image edges, nose, occlusions, and collisions of particles as discussed earlier.

A 3×3 grid point pattern (circles), the same grid displaced to the left by one interpoint distance of 15 pixels (crosses), and the resultant displacement field is shown in Fig. 3-18. A routine employing Runge-Kutta fourth and fifth order pairs is used to solve the differential equation sets. The initial values of processing elements are selected with a random number generator in the range of 0. to 0.5, in the 3 diagonals with the main diagonal centered and -.5 to 0. elsewhere. This is taken considering that "1"s in the final states of processing elements would show up in the 3 diagonals as long as there is a missing point or no missing points at all, and points are numbered in the same manner in both patterns. By doing this, the initial states, taking the sigmoid function into account, are placed closer to the desired final states than ones with the assignment of initial values by random numbers in the whole range (-0.5 to 0.5). The following values of weights for each constraint and parameters are found experimentally to be appropriate throughout the experiments with grid point patterns.

$A = B = 500$ $E = 25$

$C = 800$ $N_1 = min(M, N) + 2$

$D = 66$ $\beta = 10$

The results for two cases of rotational motion are presented in Fig. 3-19 and Fig. 3-20, respectively. In Fig. 3-19, the pattern is rotated 20 degree counterclockwise with respect to the lower left point. In Fig. 3-20, the pattern is rotated 40 degree counterclockwise with respect to the center point. It is noticeable that all three patterns are generated such that they may produce the ambiguous motions if the motion are analyzed at a local area.

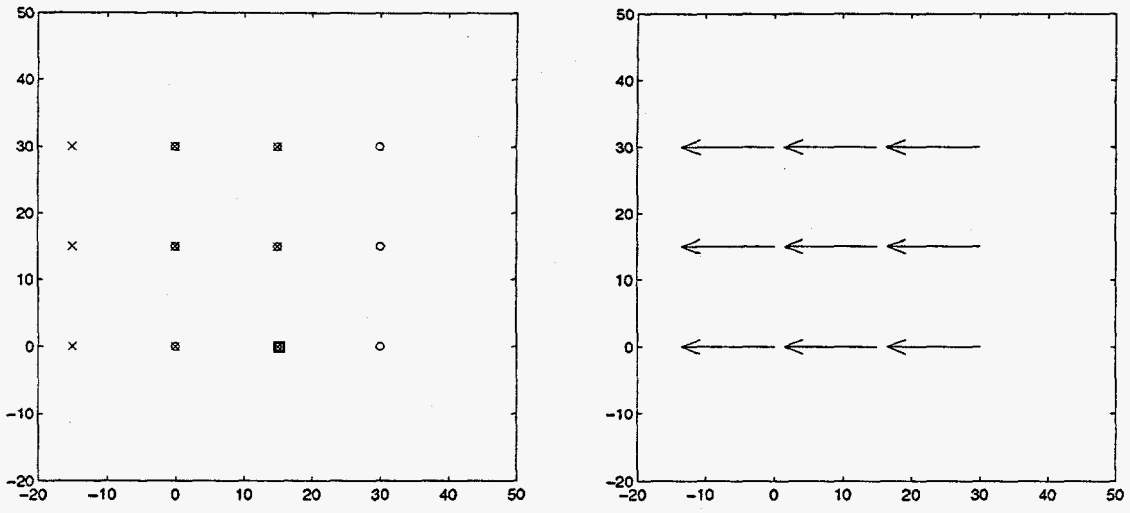

Fig. 3-18 Point patterns and resultant displacement field

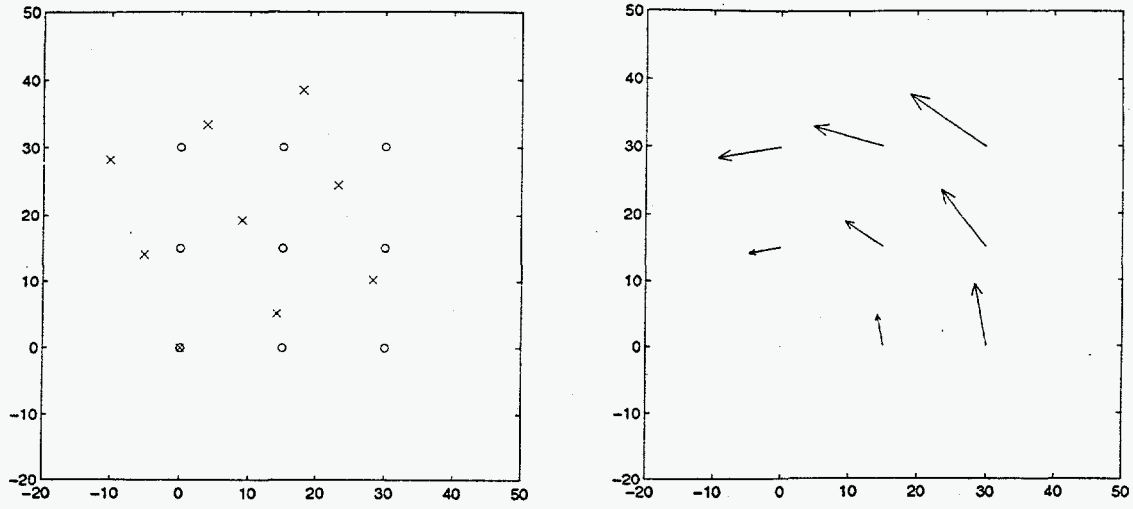

Fig. 3-19 Point patterns and resultant displacement field

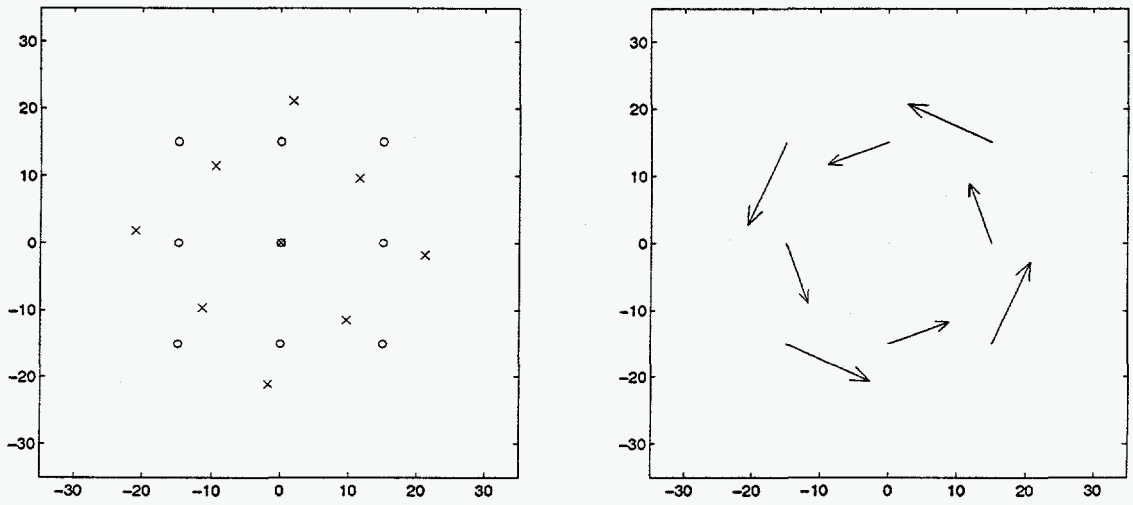

Fig. 3-20 Point patterns and resultant displacement field

In addition to the test for translational and rotational motion, the test result for the grid patterns with 10 pixels displacements to the left, random displacements up to 3 pixels in the horizontal and vertical direction for each point, and a missing point to simulate real patterns from flowing particle images is presented in Fig. 3-21.

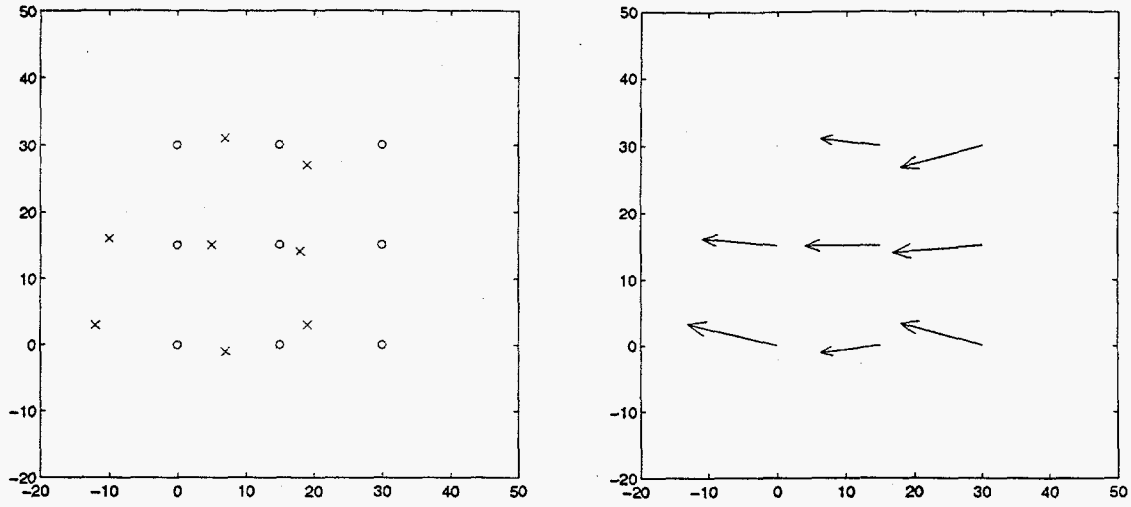

Fig. 3-21 Point patterns and resultant displacement field

The above results demonstrate that the Hopfield network makes the correspondence to the ambiguous motion by obtaining global solutions, and this method is applicable to real patterns. Also, these results show the validity of the rigidity constraint for the correspondence problem even for considerable random motions. We have monitored the performances of the point correspondence for the grid patterns with and without the rigidity constraint along with the initial value assignment scheme. These showed that the performance with the rigidity constraint and the initial value assignment scheme is better than that without the rigidity constraint or the initial value assignment scheme. Without the rigidity constraint or the initial value assignment scheme, states of processing elements do not converge to stable states for the case of displacement more than half interpoint distance whereas with the rigidity constraint and the initial value assignment scheme, the performance is improved to the extent that the solution is available for one interpoint displacement or even more as shown in the previous experiments.

Experiment 2: Point Correspondence with Real Patterns

Real point patterns from the rotating bumpy base sample and flowing acrylic particles down the inclined chute are used for this experiment. Fig. 3-22 shows two successive images, which are taken while the bumpy base is rotating clockwise on a rotating disk. The image on the left hand side precedes the image on the right hand side by a sampling time of 2 msec. The image size is 192 by 239. The point pattern in Fig. 3-23 is generated using variance normalized correlation with a threshold of 0.55 (circles for the preceding image and crosses for the current image) because brightness patterns of particles are consistent enough. There are some points in the patterns that have no correspondence due to the image edges, noise in the images. Since we have lots of points in both patterns, it would take tremendous amount of time to obtain a final solution if we compute the correspondence with the total number of points. In order to speed up the computation, we try a windowing scheme over the total area of the patterns. The total area of the patterns is divided into rectangular areas of size, 40 by 40 pixels such that neighboring areas overlap each other by 10 pixels. This scheme provides correspondences for the missing points caused by the partition of the total image because the correspondences are updated as the rectangular area is shifted with the overlap. The initial values are selected with a random number generator in the range of - 0.5 to 0.5, which is shown to produce the best match all the time. The following values of weights for each constraint and parameters are found experimentally to be appropriate for this problem.

$A = B = 500$ $E = 40$

$C = 800$ $N_1 = min(M, N) + 2$

$D = 270$ $\beta = 10$

The weight values of C and D are chosen differently from the previous experiment. It is found that the initial values of processing elements and the weight values of constraints have to be decided depending on specific problems.

The displacement field is presented in Fig. 3-24. Except one point near the top right corner, the correspondence is solved as supposed to be.

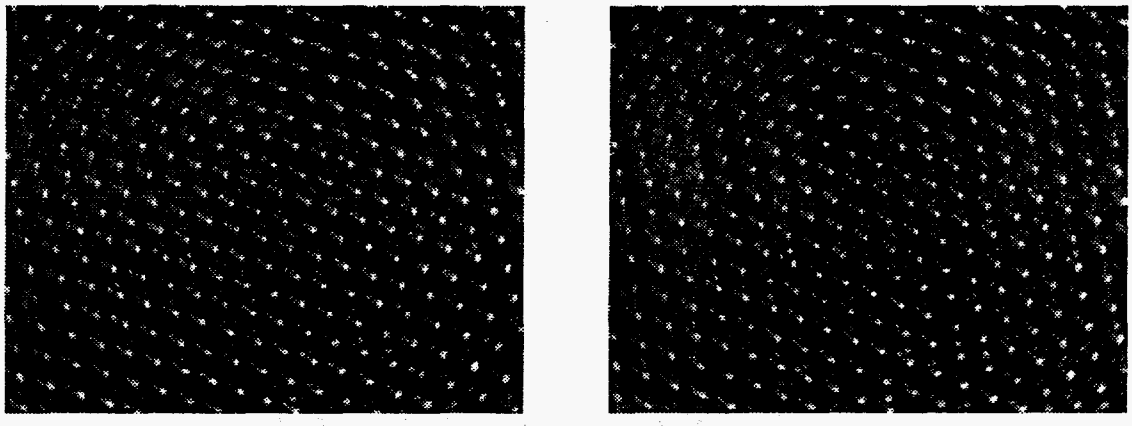

Fig. 3-22 Two successive images

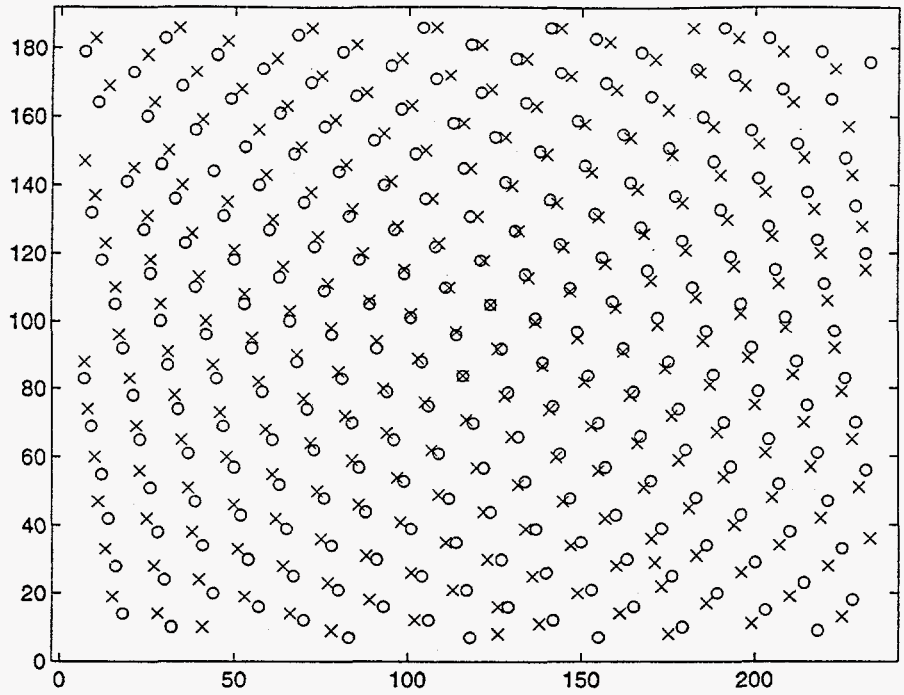

Fig. 3-23 Point patterns

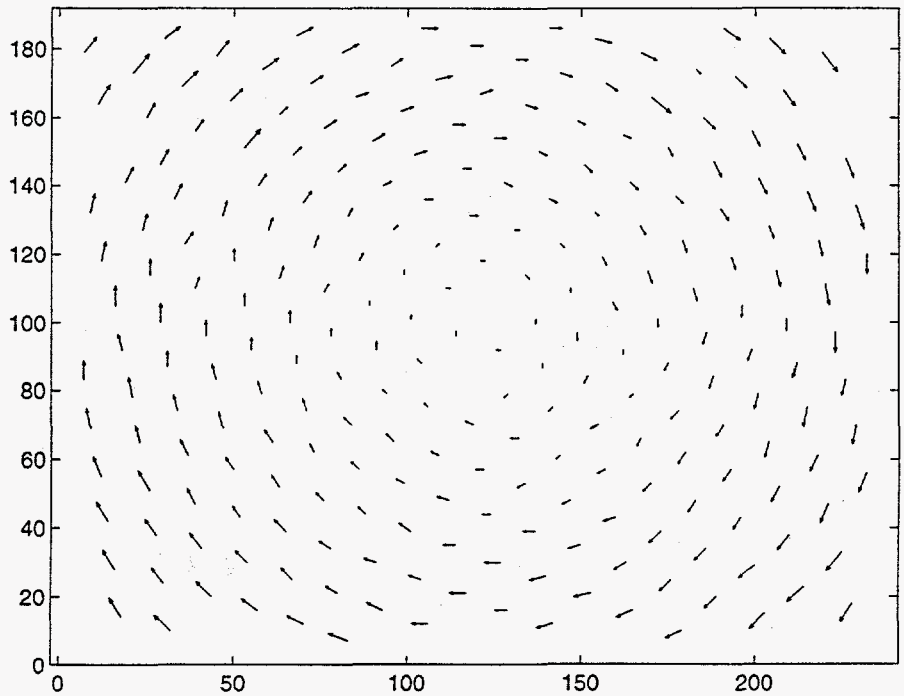

Fig. 3-24 Displacement field

Now, we are going to apply the point correspondence to the real point pattern derived from flowing acrylic particles down the inclined chute. The point patterns in Fig. 3-15 obtained with the preprocessing are used for this experiment. There are four points in the patterns (one marked by circles and three marked by crosses) that have no correspondence due to the image edges, noise in the images and occlusions of particles. The number of circles is 39, and the number of crosses is 41. Using the windowing scheme described in the previous experiment, the total area of the patterns is divided into four rectangular areas such that neighboring areas overlap each other by 10 pixels. The diameter of a particle image is typically 12 pixels. The images are taken with sufficient speed to ensure that particles move less than one diameter between successive images. The initial values are selected with a random number generator in the range of - 0.5 to 0.5, as in the previous experiment. The following values of weights for each constraint and parameters are found experimentally to be appropriate for this problem.

$A = B = 500$ $\qquad$ $E = 73$

$C = 800$ $\qquad$ $N_1 = min\,(M, N) + 2$

$D = 160$ $\qquad$ $\beta = 10$

Fig. 3-25 shows that the correspondence is solved for all points including missing points, as expected, and the velocity field for each particle is derived at subpixel resolution. Since the point correspondence is solved by the Hopfield network, the image areas corresponding to preceding points are correlated with the image areas corresponding to current points. The image data of the areas are weighted by a Gaussian window to extract

the image data of a particle as discussed earlier. Polynomial interpolation by 10 is applied to 3 by 3 points with the current points centered. Then, displacements corresponding to maximum values in the interpolated planes are searched for. The velocity field in Fig. 3-25 shows the subpixel resolution velocities even where two points in successive frames coincide.

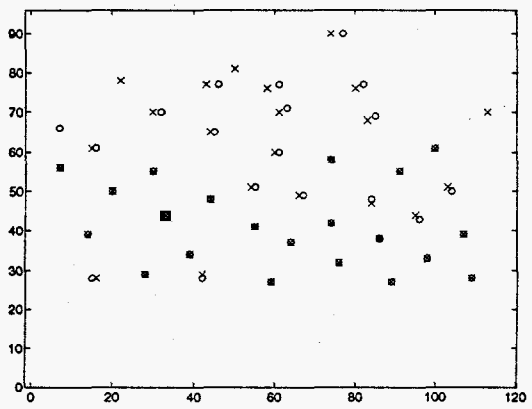

Fig. 3-15 Point patterns

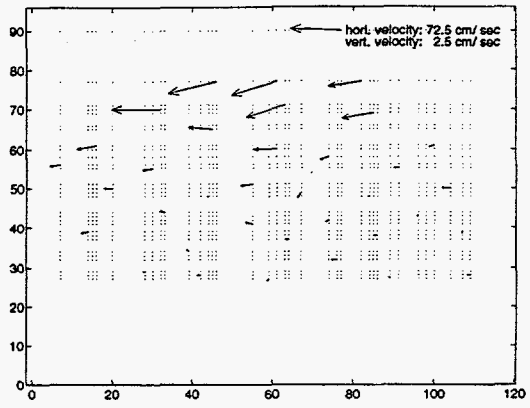

Fig. 3-25 Velocity field

CHAPTER 4
APPLICATION TO FLOW DOWN AN INCLINED CHUTE

We have observed a variety of flow regimes in the chute, with remarkable differences in their nature. Examples of these flows include highly energetic flows in which the concentration is low and collisions are dominant. Other flows include quasi-static sliding at high concentrations, rapid sliding at intermediate concentrations, and saltation at low concentrations. The steady, fully developed flows and some waves at the free surface also have been observed as inclination is changed with the same entrance gate height. More than one type of flow can be obtained at the same angle of inclination, depending upon the entrance conditions and the material characteristic of the base.

The steady and wavy flows of glass particles down the bumpy base are studied in this chapter. The velocities and temperatures of both steady and wavy flows are measured and compared using the correlation introduced in chapter 2. The measurements are qualitatively compared with Richman and Marciniec's theoretical model. Also, the volume fraction of flowing acrylic particles is measured.

Experimental Results

Experiments are conducted in a flow simulation system which consists of a inclined chute, a conveyer for particle recirculation, an upper hopper for granular storage and a lower hopper for guiding the discharge to the conveyer. The flow region of the

experimental apparatus consists of a rectangular aluminum chute with transparent side walls. The interior of the chute is 4 m long, 45 cm tall, and the width is adjustable from 0 to 25 cm in 2.5 cm increments. The base of the chute is designed to be covered with interchangeable inserts, allowing different base roughness conditions to be studied; in these experiments the base consists of 3 mm glass particles fixed in a closely spaced hexagonal pattern (bumpy base). The inclination angle of the chute is adjustable between 0 and 35 degree. An adjustable gate apparatus at the entrance of the chute controls the entering flow. A series of flow-trapping gates are developed to measure the mass hold-up in six sections along the chute. These gates fall under the influence of gravity when holding pins are simultaneously removed by a solenoid driven piston. The particles used in these experiments are glass spheres with diameters of approximately 3 mm.

A series of experiments showed that the steady (angle, 23 degree) and wavy flow (angle, 21.5 degree) were generated under the following conditions: chute width, 15 cm; entrance gate height, 5 cm. Thus, we investigate the behavior of the flows for these cases.

We measure the flow rate, flow thickness and mass hold-up. The flow rate is measured by weighing the mass in marked sections of the conveyor belts that delivers the particles from the exit to the entrance of the chute. The mass hold-up is a measurement of the amount of flow in the chute at any instant. This is performed by dropping the gates in the chute simultaneously, trapping the flow in six sections. The mass hold-up can be combined with flow thickness and flow rate measurements in order to calculate the average volume fraction and velocity in each of the six sections. The volume fraction is a measure of the fraction of flow occupied by particles. Table 4-1, Fig. 4-1, Fig. 4-2, Fig. 4-3 and Fig. 4-4 show the flow rate, flow thickness, mass hold-up, volume fraction and velocity measure-

ments for the steady and wavy flow, respectively. Section number 2 refers to flow area closest to the entrance, and section number 7 refers to the flow area next to the exit. The rest of sections are numbered in order. The flow rate, mass hold-up and velocity measurements are dimensionless using the factors of $\rho dw\sqrt{gd}$, ρd and $\sqrt{gd}$, respectively where d is the particle diameter of 0.3 cm, and ρ is the particle density of $2.5\,e-3\,\mathrm{kg/cm^3}$, and w is the chute width of 15 cm, and g is the gravity of 981 $\mathrm{cm/sec^2}$.

Table 4-1 Flow rate measurement

	Steady flow (angle, 23 degree)	Wavy flow (angle, 21.5 degree)
Flow rate (dimensionless)	16.46	15.06

Velocity and Temperature Measurements of Flowing Glass Particles

Variance normalized correlation is applied to the images of flowing glass particles to measure the velocity and temperature. The mean square value of the random velocity is commonly referred to as temperature defined as $T = \frac{1}{3}(\langle u'^2\rangle + \langle v'^2\rangle + \langle w'^2\rangle)$ where u', v', w' are instantaneous velocity fluctuations. Since the correlation produces 2-dimensional velocity measurements in the image plane, the temperature is derived from 2 velocity components ($T = \frac{1}{2}(\langle u'^2\rangle + \langle v'^2\rangle)$).

The images are taken from the side wall and the top of the chute. The side and top-view images have been taken about 0.8 m (section 6) and 1.7 m (between section 4 and 5) upstream of the chute outlet, respectively. The camera is operated to take a pair of images

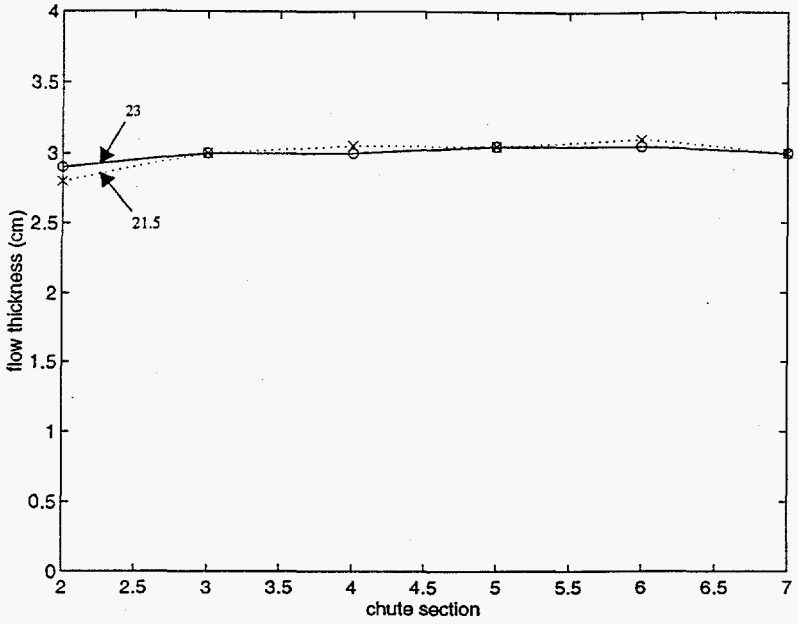

Fig. 4-1 Flow thickness

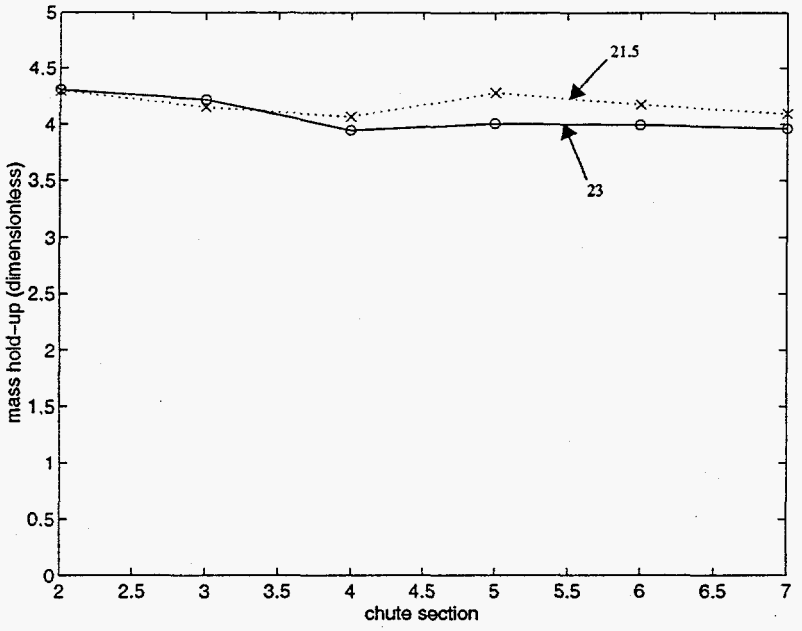

Fig. 4-2 Mass hold-up

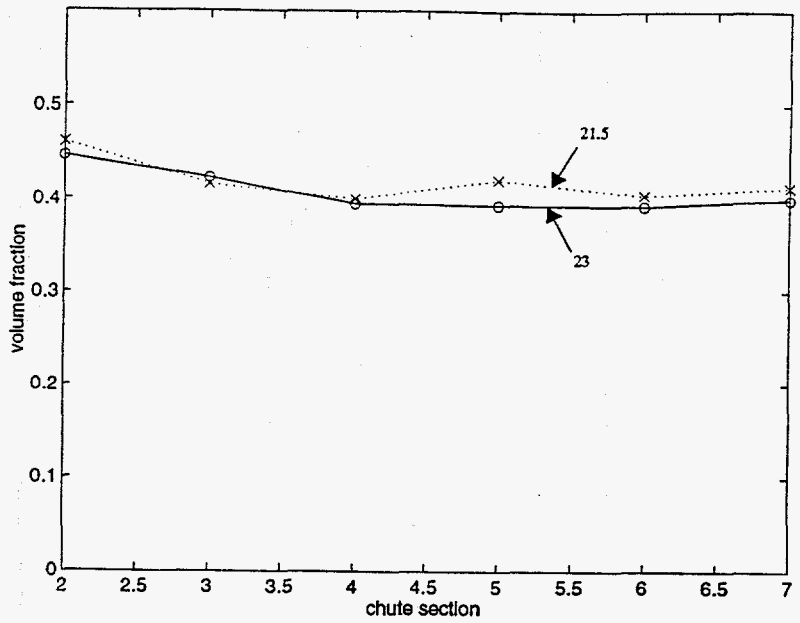

Fig. 4-3 Volume fraction

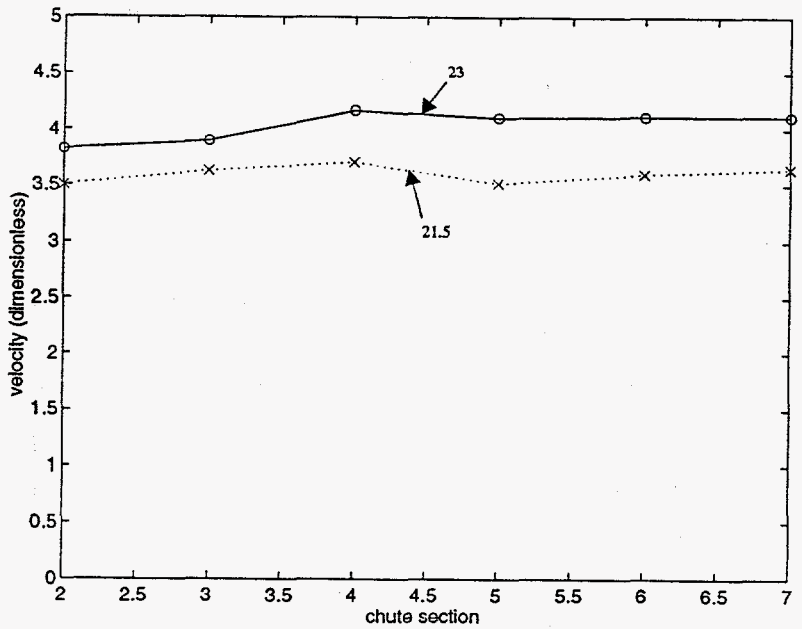

Fig. 4-4 Velocity

every 0.25 second for total 272 pairs of images, by which the images are taken for 67.75 second. The sampling time of 0.25 second is decided in consideration of the range of observed wave period (order of second or more). The images are taken with the sampling rate of 1000 frames/ sec, by which the time lag between images in a pair is 1 msec. We first illustrate instantaneous velocity measurement using a pair of images, then present average velocity and temperature measurement using the total 272 pairs of images for the steady (angle, 23 degree) and wavy flow (angle, 21.5 degree), respectively.

Fig. 4-5 shows a pair of successive images taken from the side wall for the steady flow (angle, 23 degree). The image on the left hand side precedes the image on the right hand side by the sampling time of 1 msec. The image areas occupying the ruler are not used for the velocity measurements. The ruler (cm scale) in the images provides the flow thickness measurement from the reference of the flow height described in chapter 2. The dark strip at the bottom of the images is the perforated aluminum plate, and the particles on the top of the plate are fixed ones (boundary particles). The distance between the reference of the flow height and the top of fixed particles is 4 mm.

The velocity field and velocity profile are presented in Fig. 4-6. The measurements use the correlation with the interpolation. Also, a threshold of 0.65, decided experimentally, is applied to the correlation to get consistent measurements. The velocity profile is derived from the average velocity field of each row. The missing vectors in the velocity field are caused by abrupt change of the brightness pattern at some locations, where correlation values are less than the threshold. The values in the velocity profile refer to the horizontal average velocities, the vertical average velocities and number of data used for the average from each row of the velocity field, respectively. The velocity measurements are

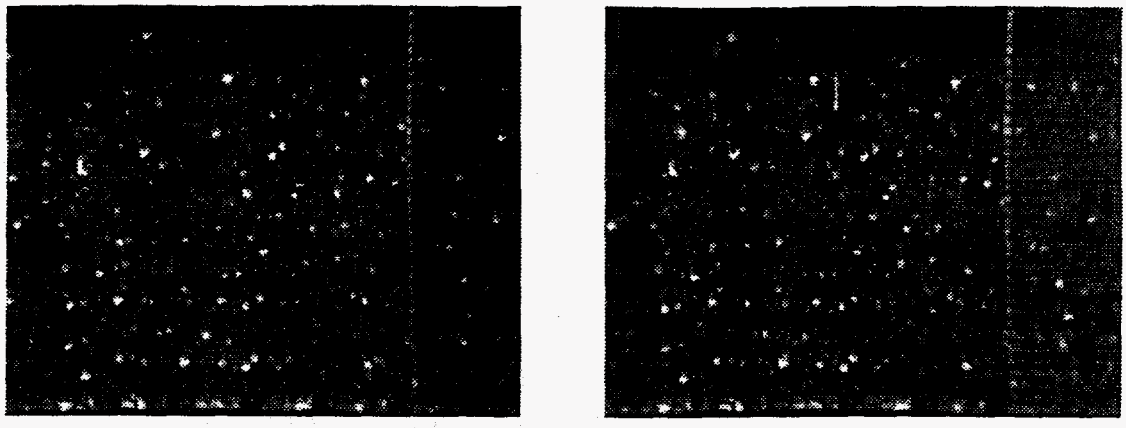

Fig. 4-5 Two successive Images

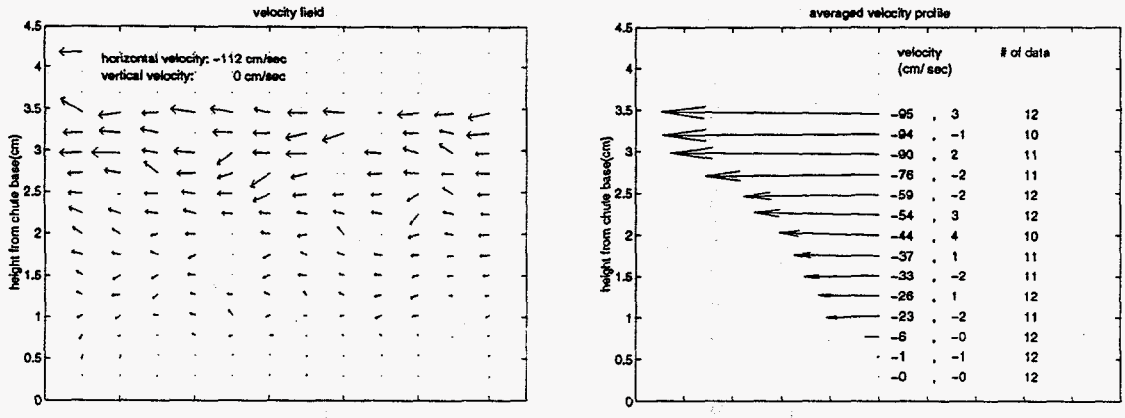

Fig. 4-6 Velocity field and profile

presented such that rightward and upward motions produce positive horizontal and vertical velocities, respectively.

The correlation method is used next with another pair of successive images in Fig. 4-7, taken from the top of the chute for the steady flow (angle, 23 degree). The images are taken such that the top and the bottom edge coincide with the interface between the flow and the side walls. The distance between the flow and camera lens is greater than the pre-

vious case in order to contain the whole width of the chute. This leads to smaller particle image size. The velocity field and the velocity profile along width of the chute are presented in Fig. 4-8. The correlation is taken with the interpolation. Also, the threshold of 0.65 is applied to get valid measurements. The velocity profile is derived in the same manner as the previous case.

The gradient in both results are caused by the friction at the chute base and at the side walls, respectively. The characteristics of these profiles are similar to those found for fluids.

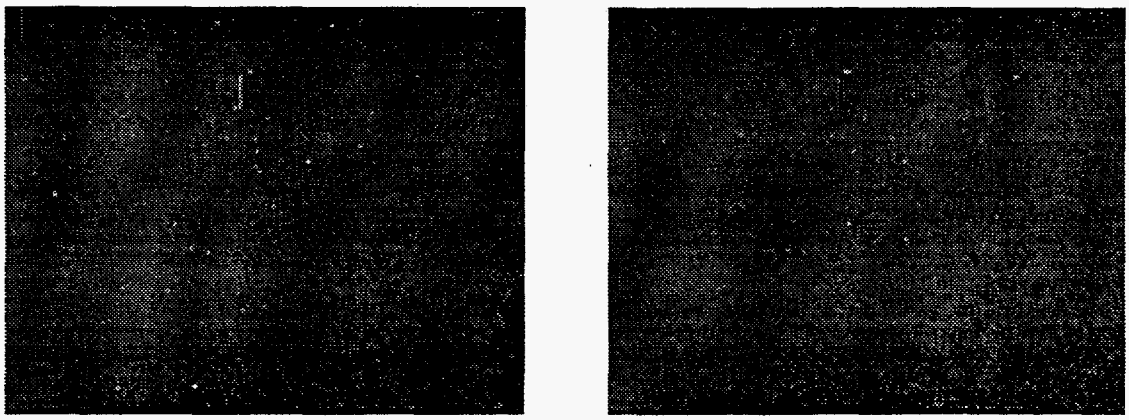

Fig. 4-7 Two successive Images

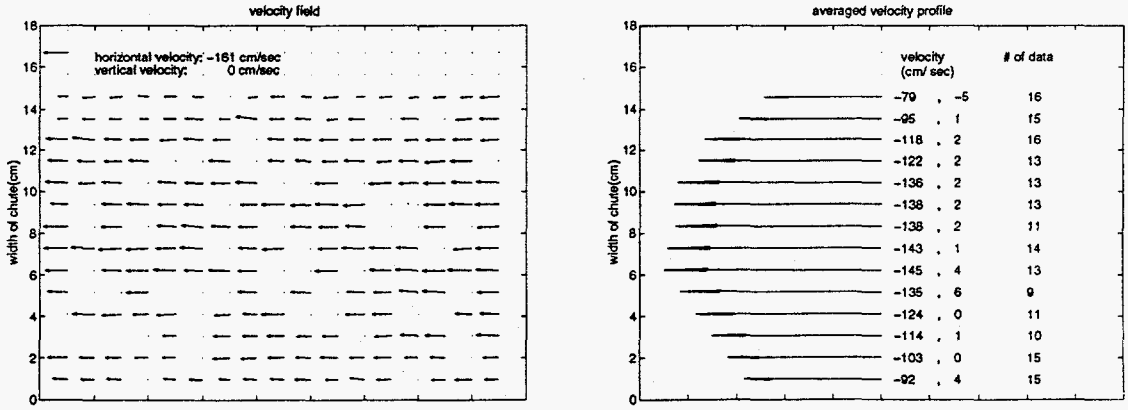

Fig. 4-8 Velocity field and profile

The instantaneous velocity measurements described above are averaged for total pairs of images (67.75 sec) for the steady and wavy flow. The average is taken for the velocity fields of each row using the same threshold. Fig. 4-9 and Fig. 4-10 show the average velocity profile from the side-view images for the steady and wavy flow, respectively. In the velocity profile for the wavy flow as shown in Fig. 4-10, the number of data at the top of the flow is much less than the numbers of data below whereas in the steady flow as shown in Fig. 4-9, the number of data at the top of the flow is comparable to the numbers of data below. The less number of data at the top of the flow demonstrates the existence of the wave in the flow. Fig. 4-11 and Fig. 4-12 show the average velocity profile from the top-view images for the steady and wavy flow, respectively.

The temperature measurements from side-view images and top-view images are produced by calculating sample variances as shown in Fig. 4-13 and Fig. 4-14, respectively. The horizontal and vertical velocity measurements are used in the temperature profiles.

In order to quantify the wave in the flow in terms of the velocity measurement, the velocity variation over total 272 top-view image pairs is monitored by averaging velocity measurements at the center of the images (7 and 8 rows of the velocity fields). Fig. 4-15 and Fig. 4-16 show the velocity variation and its FFT for the steady flow (angle, 23 degree). Fig. 4-17 and Fig. 4-18 show the velocity variation and its FFT for the wavy flow (angle, 21.5 degree). The means of the velocity variations are subtracted from the velocity variations in order to eliminate DC components, by which the low frequency content can be clearly represented. Then, 512 FFT is taken for the representation of the velocity variations in the frequency domain. The frequency representation of the velocity variation for

the steady flow shows wide band, whereas that for the wavy flow shows narrow band relatively. This means that the velocity variation in the steady flow occurs randomly, however the velocity variation in the wavy flow occurs periodically. From the frequency representation of the velocity variation for the wavy flow as shown in Fig. 4-18, the period of wave in the flow turns out to be about 2.5 second.

Volume Fraction Measurement of Flowing Acrylic Particles

We generated the point patterns (Fig. 3-14) from acrylic particle images in chapter 3. Counting the number of particles in a point pattern may produce a basis for volume fraction measurement. Thus, the image area is divided into particle size (12 pixels) vertically, and the number of particles for every vertically divided area are counted for the volume fraction measurement. Since the images are taken from the side wall for this measurement, the measurement produces the volume fraction only for flow region occupied particles right next to the side wall. The point pattern from the left image in Fig. 3-13 is used for this measurement, and the resultant volume fraction are presented in Fig. 4-19. The volume fraction measurement turns out to be similar to the theoretical volume fraction profile as will show later even though the acrylic particles are not so elastic as particles in the theoretical model.

The method of volume fraction measurement is stimulated by Drake's method (Drake 1991). Drake divided the images into bed-parallel layers or bins two particle diameters thick, and manual measurements such as the mean velocities and bulk density were taken for each bin. Manually counting particles for the density measurement would be tedious, time-consuming, and inaccurate. However, variance normalized correlation can

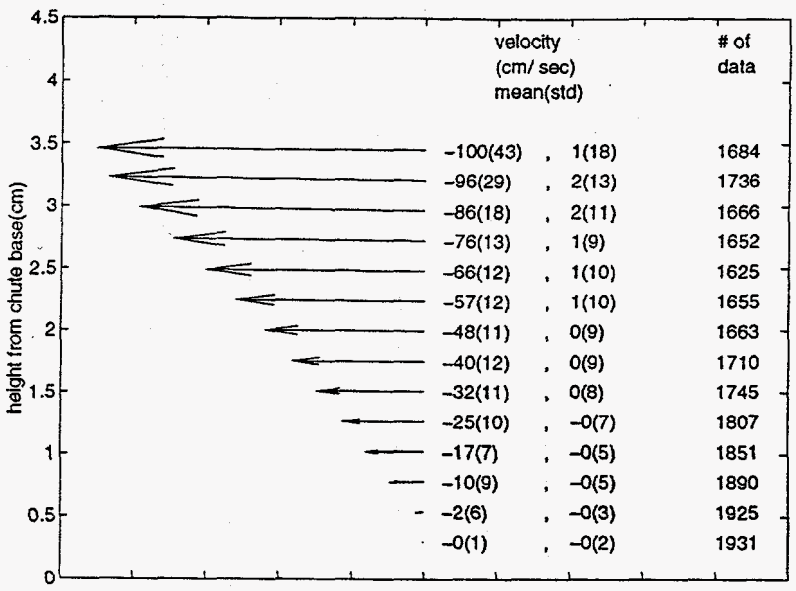

Fig. 4-9 Average velocity profile (angle, 23 degree)

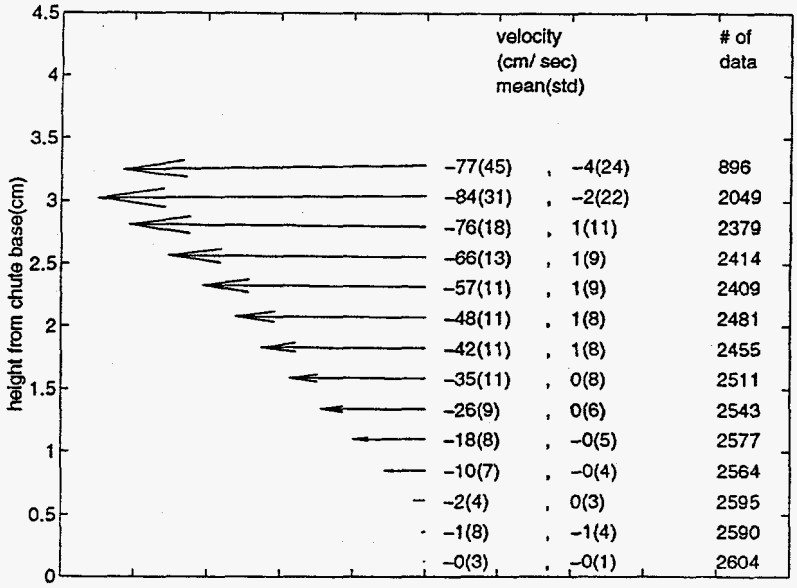

Fig. 4-10 Average velocity profile (angle, 21.5 degree)

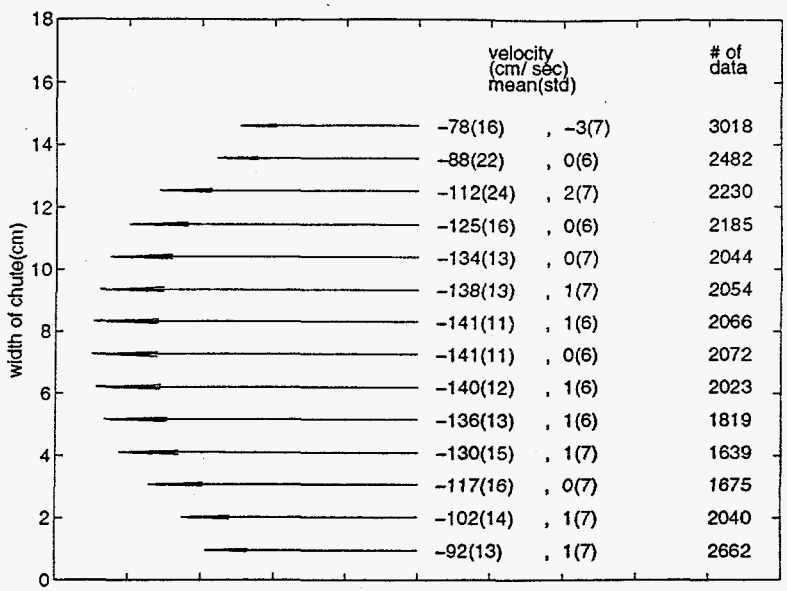

Fig. 4-11 Average velocity profile (angle, 23 degree)

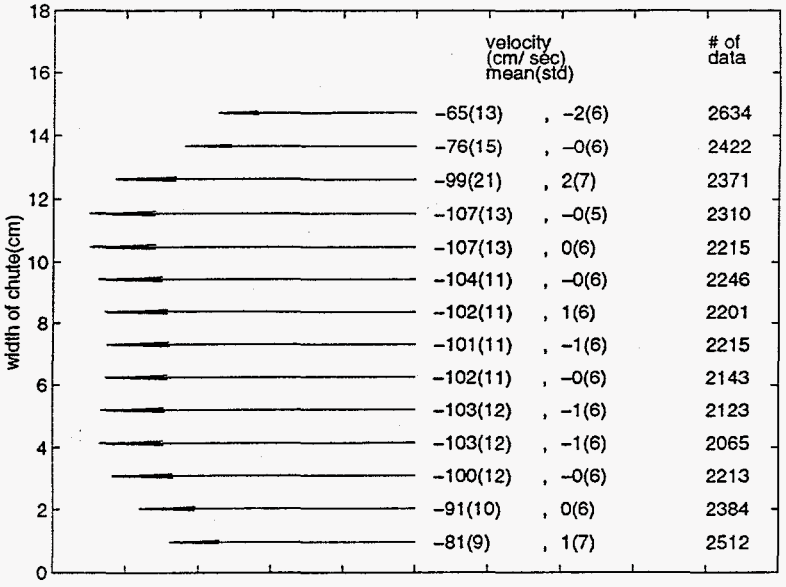

Fig. 4-12 Average velocity profile (angle, 21.5 degree)

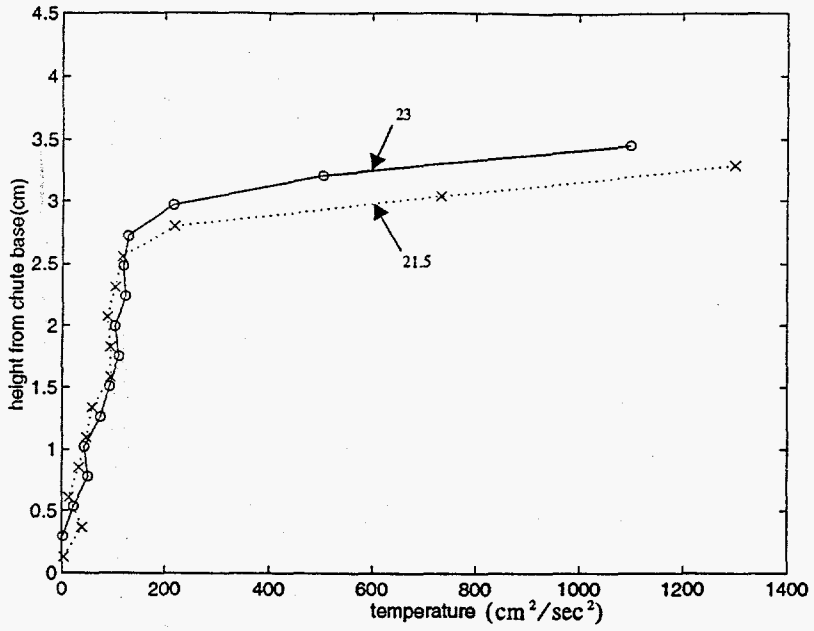

Fig. 4-13 Temperature profiles

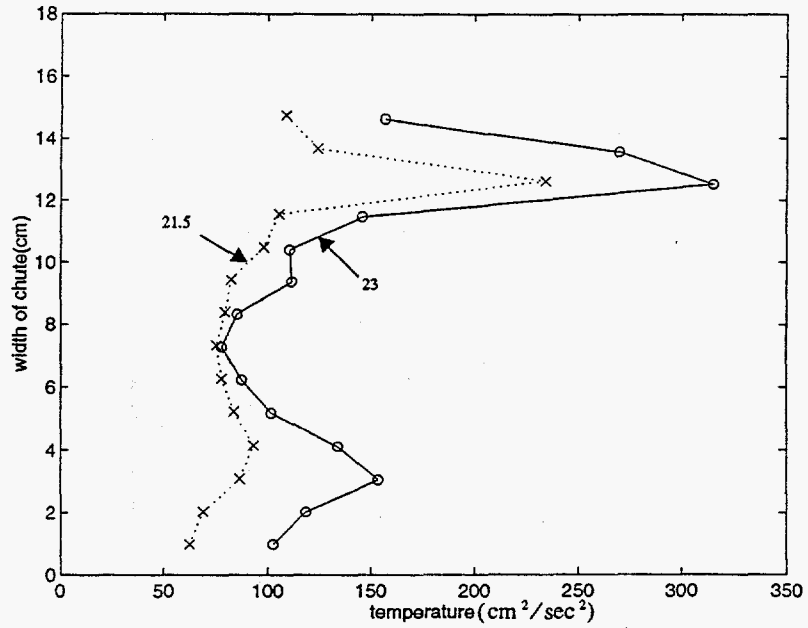

Fig. 4-14 Temperature profiles

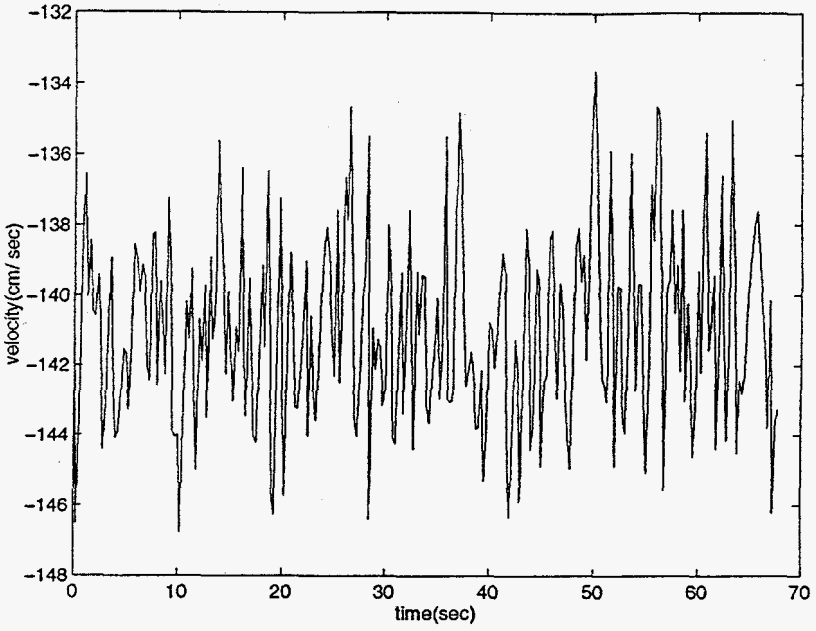

Fig. 4-15 Velocity variation (angle, 23 degree)

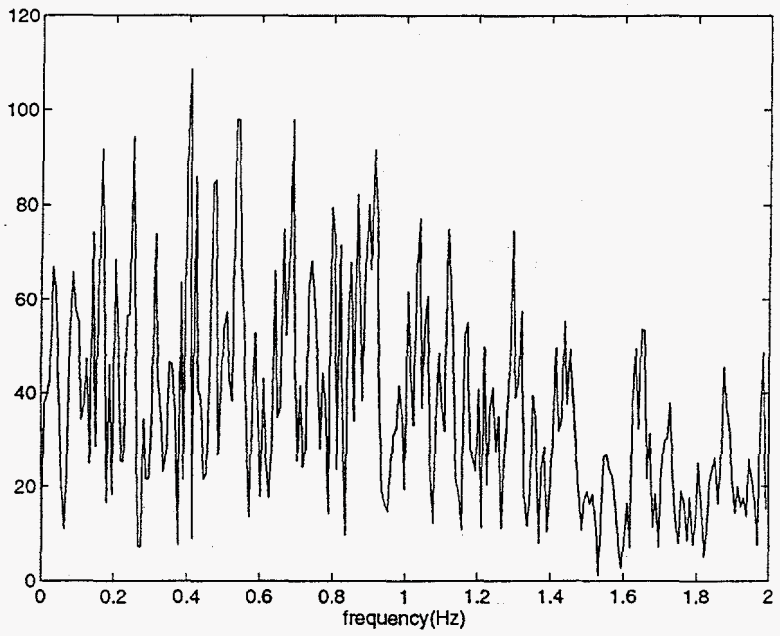

Fig. 4-16 FFT of velocity variation (angle, 23 degree)

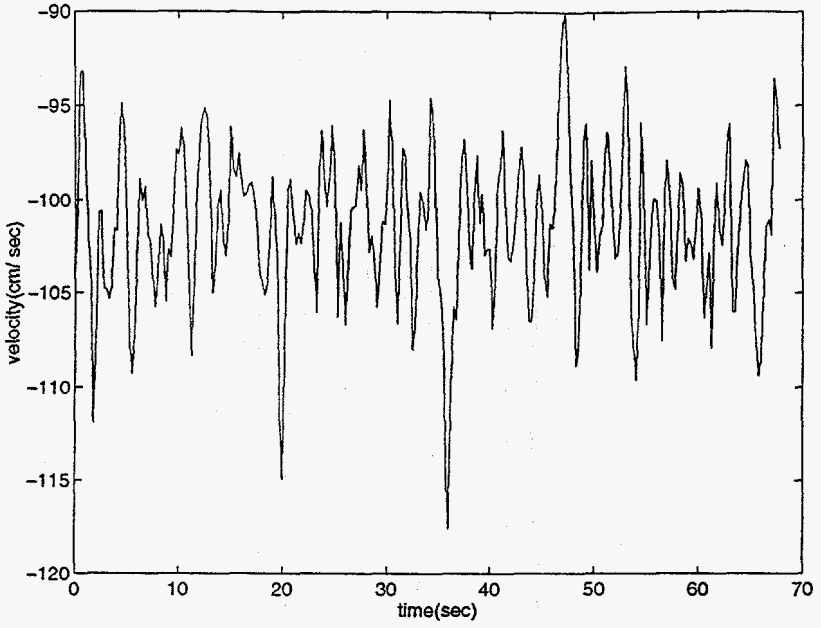

Fig. 4-17 Velocity variation (angle, 21.5 degree)

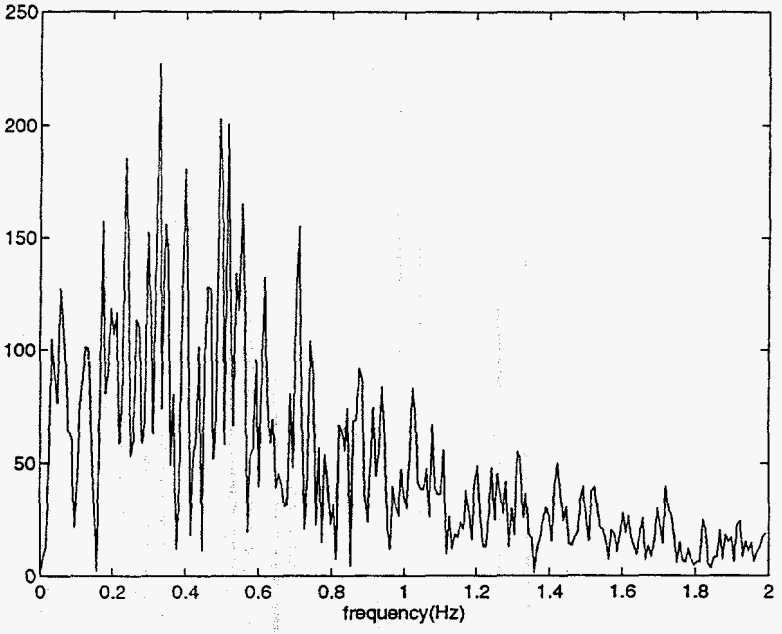

Fig. 4-18 FFT of velocity variation (angle, 21.5 degree)

recognize every acrylic particle in the images as demonstrated in chapter 3. It is very straightforward to count particles using a computer in a well defined point pattern. Thus, the newly developed method produces more reliable and accurate volume fraction measurement automatically. Moreover, it is expected that the fluctuating velocity (temperature) can be measured in the same manner if large number of images are used.

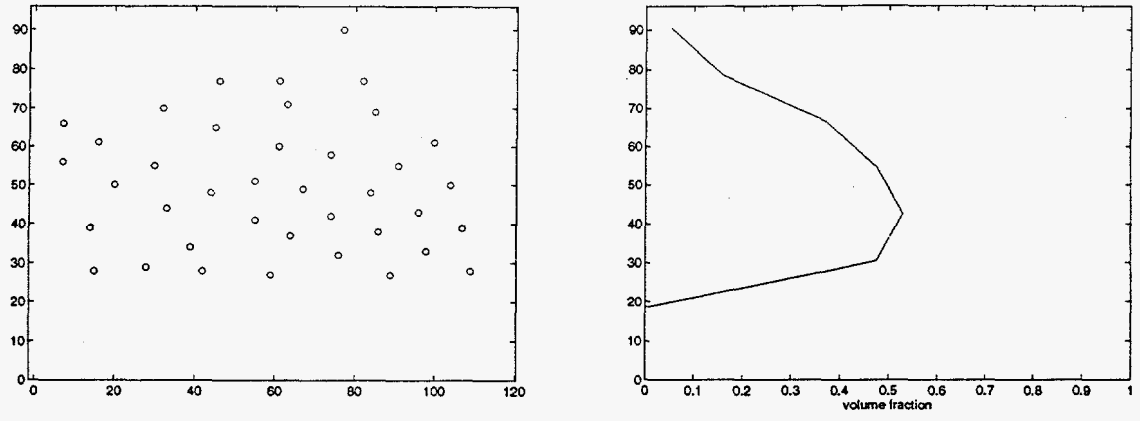

Fig. 4-19 Point pattern and volume fraction measurement

Theoretical Model of Granular Flow down Bumpy Inclines

Richman and Marciniec (1990) developed a theoretical model of gravity driven granular flows down bumpy inclines with an inclination angle ϕ as shown in Fig. 4-20. The particles are characterized by mass m; diameter σ; and coefficient of restitution between flow particles, e. The mean fields of interest are the volume fraction, ν; the mean velocity, $\boldsymbol{u}$, about which the particles fluctuate; the granular temperature, T.

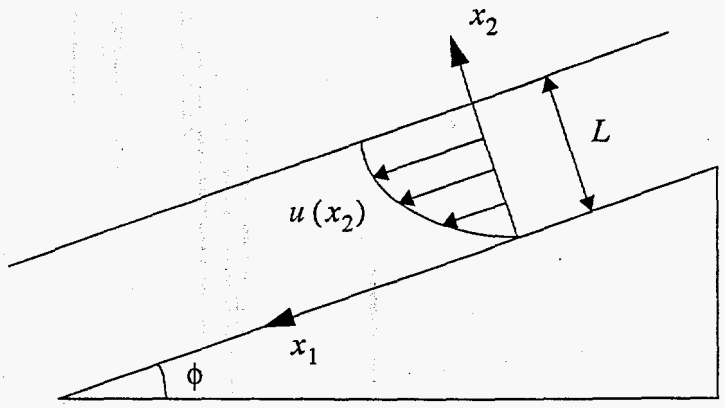

Fig. 4-20 Sketch of granular flow down an incline

The model is based on the balance equations for mass, momentum, and the fluctuating energy:

$$\dot{\rho} + \rho \nabla \bullet \boldsymbol{u} = 0 \tag{4.1}$$

where an dot indicates a time derivative following the mean motion;

$$\rho \dot{\boldsymbol{u}} = -\nabla \bullet \boldsymbol{P} + \rho \boldsymbol{g} \tag{4.2}$$

where $\boldsymbol{P}$ is the pressure tensor and $\boldsymbol{g}$ is the body force unit mass; and

$$(3/2)\,\rho \dot{T} = -\nabla \bullet \boldsymbol{Q} - tr(\boldsymbol{P} \bullet \boldsymbol{D}) - \gamma \tag{4.3}$$

where $\boldsymbol{Q}$ is the flux of fluctuating energy, γ is the collisional rate per unit volume of energy dissipation, and $\boldsymbol{D}$ is the symmetric part of the velocity gradient $\nabla \boldsymbol{u}$.

The bumpy boundary is a flat surface to which particles of diameter d are randomly attached as shown Fig. 4-21. When a flow particle collides with a boundary particle, the distance between their centers is $\bar{\sigma} = (\sigma + d)/2$. Dimensionless measures of boundary geometry are $r = \sigma/d$ and $\Delta = s/d$. The bumpiness of the boundary is characterized by an angle, $\theta = \text{asin}\left((1+\Delta)/(1+r)\right)$. The boundary coefficient of restitution is e_w that characterizes the energy dissipated in the boundary -flow particle collision.

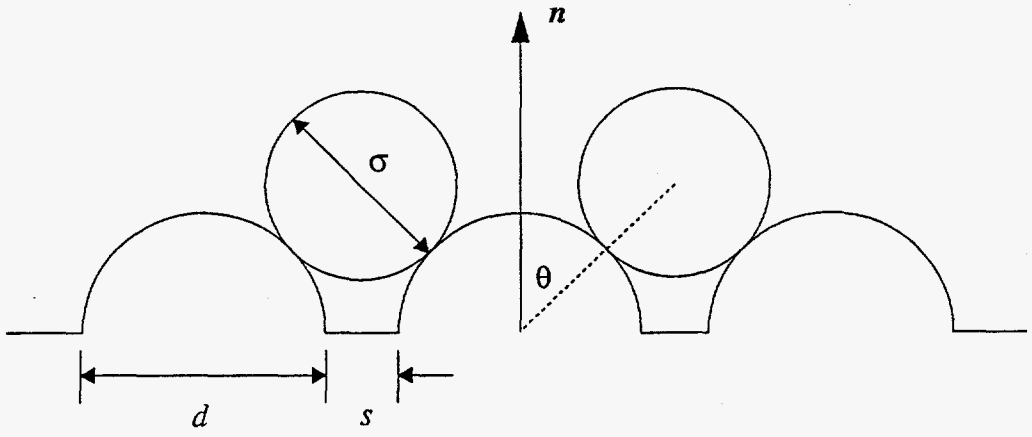

Fig. 4-21 Geometry of the bumpy boundary

Steady, fully developed, gravity driven granular flows down bumpy inclined surfaces are investigated. The gravity is g, the angle between the incline and the horizontal is ϕ, and the perpendicular distance from the incline to the free surface is L as shown in Fig. 4-20. An $x_1 - x_2 - x_3$ Cartesian coordinate system is introduced, in which x_1 measures parallel distances along the incline and x_2 measures perpendicular distances above the

incline. By adopting the dimensionless coordinate, $y = (L - x_2)/\sigma$ measured from the free surface and assuming that the flows are infinitely extended in the x_3-direction, the volume fraction, ν; the dimensionless velocity, $u = u_1/(\sigma g)^{1/2}$; and the dimensionless temperature, $w = (T/\sigma g)^{1/2}$ depend on y only. The typical mean fields of interest based on this model are closely reproduced to show the variation of the volume fraction, temperature, and velocity with the height of the flow in Fig. 4-22, Fig. 4-23, and Fig. 4-24, respectively. These reproductions are made for $\bar{\nu} = 0.27$, $\phi = 20$ degree, $e = 0.8$, $e_w = 0.95$, $\dot{m} = 50$, $r = 1/2$ and $\Delta = -1 + \sqrt{2}$.

The $\bar{\nu}$ is depth-averaged solid fraction,

$$\bar{\nu} = (1/\beta)\int_0^\beta \nu \, dy \tag{4.4}$$

where β is the dimensionless depth at the base ($\beta = L/\sigma$), and $\dot{m}$ is the mass flow rate defined by

$$\dot{m} = \int_0^\beta \nu u \, dy. \tag{4.5}$$

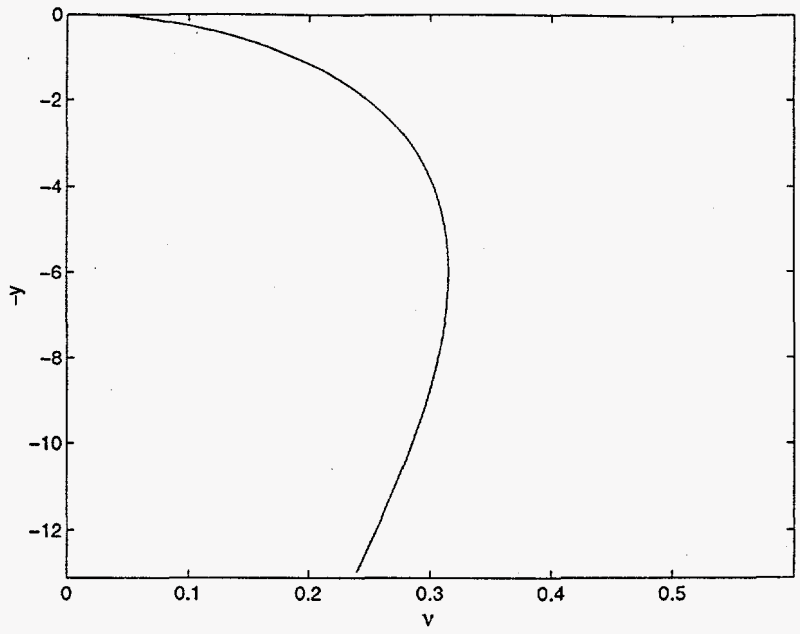

Fig. 4-22 Volume fraction profile

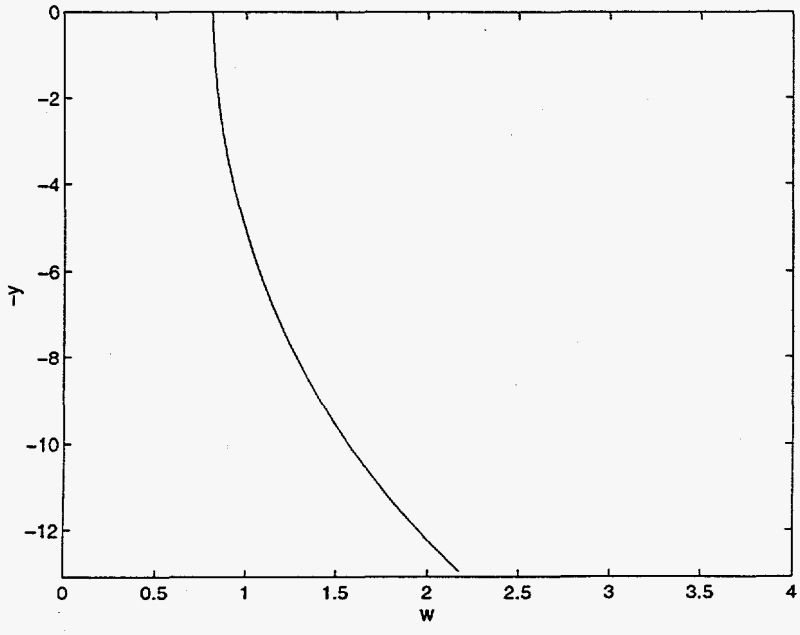

Fig. 4-23 Temperature profile

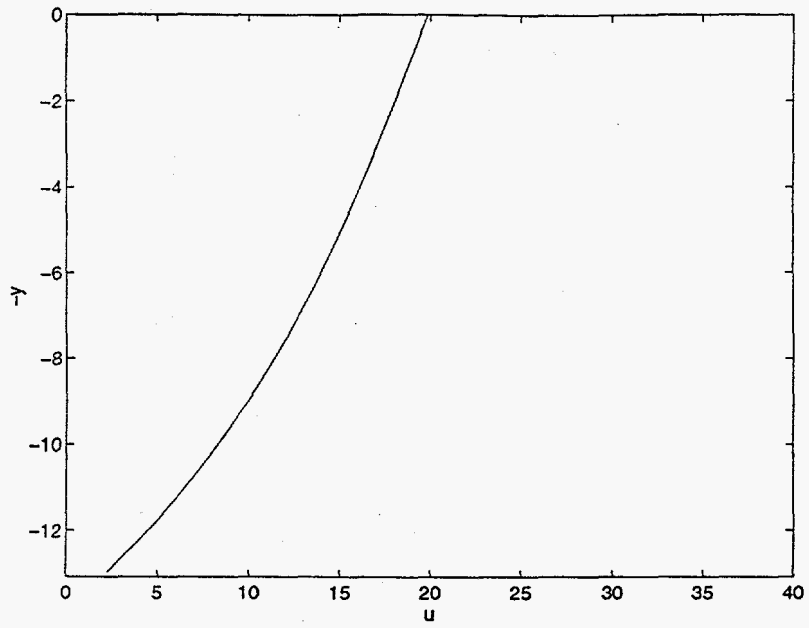

Fig. 4-24 Velocity profile

Discussion

It is found that the temperature profiles based on the theoretical model are different from the experimental measurements: the theory shows that the temperature decreases as the flow height goes up, whereas the experimental measurements show the opposite. In other words, the theory says that the temperature is generated at the bumpy boundary, whereas the experimental measurements say that the temperature is dissipated at the boundary. It is observed with visual inspection that particles at the around bottom interact frictionally with neighbors over long periods of time (quasi-static regime) whereas particles interact more collisionally with neighbors as particles are at higher location (rapid-flow regime). Also, particles which interact with the bumpy base tend to be trapped in the dents formed by fixed particles to the base (boundary particles), and particles at the top of

flows move in a saltation mode. According to the mechanisms of temperature generation mentioned earlier, the high temperature at the top of flows is expected behavior: based on the visual inspection, the temperature generation due to the collisions and streaming is more probable as particles are at higher location.

In the temperature measurements from top-view images, the high temperatures occur at about 3 and 13 cm from the reference of the chute width for both steady and wavy flow. It is noticeable that the velocity gradients at the same locations are steeper than other locations. Accordingly, the high temperatures may be explained by the fact that the magnitude of temperature is proportional to the local velocity gradient.

Since the side and top-view images are not taken for the same flow region as described earlier, it is not appropriate to compare the measurements from both images in general. However, the steady flow (angle, 23 degree) appears to be fully developed based on the flow thickness (Fig. 4-1), mass hold-up (Fig. 4-2), volume fraction (Fig. 4-3) and velocity measurement (Fig. 4-4) from the flow region between the section 4 and 5 (top-view images) to the section 6 (side-view images). Thus, it is comparable for the steady flow. The comparison between averaged velocities measured from side and top-view images shows discrepancy of velocity at the wall for the steady flow. The velocity at the bottom of the velocity profile from top-view images has to be compared with that at the top of the corresponding velocity profile from side-view images according to the imaging setup. As a possible reason for the discrepancy, particles at the top of the flow in the side-view images may locate away from the wall, which causes errors in velocity measurements due to the different scale factor between the physical size of a particle and the image size occupied by the particle.

As mentioned earlier, the overall trend of the temperature profile in the theoretical model is different from that in the experimental measurements. Since the velocity profile is derived from an integration of the temperature profile in the theoretical model (Richman and Marciniec 1990), it is not appropriate to compare the experimental measurements with the theoretical model directly. Besides, it is found that there are differences between the assumptions of the theoretical model and the experimental setup. In the theoretical model, it is assumed that the flows are infinitely extended in depth ($x_3$direction), however in the experimental setup, the flows are confined by the two walls. In other words, the theory simplified the flows by modeling the flows 2-dimensionally, however the experimental flows are 3-dimensional flows as demonstrated by the velocity gradients in the top-view images. On the other hand, the theory models the boundary 2-dimensionally with the randomly attached boundary particles, which should be modelled 3-dimensionally and take regularity of boundary particles into account for direct comparison.

CHAPTER 5
CONCLUSION

We propose techniques utilizing digital images to estimate the dynamics of flowing grains down an inclined chute under the action of gravity. Variance normalized correlation as a block matching technique is employed to evaluate the spatially averaged velocities of glass particles. The resolution of this method is improved to 1/10 pixel by interpolation.

This method is evaluated with three test cases. The first case is an artificial image displaced at the subpixel resolution arbitrarily. The image consists of a 2-D Gaussian function to simulate the brightness pattern of a particle in images. It turns out that the result of the correlation without interpolation is a rounded off version of the real displacement, and correlation with interpolation produces the measurements with the accuracy of 1/10 pixel. The second and third case are images of glass particles flowing down the inclined chute. The estimated velocities compare within 1 pixel with manual particle tracking and are consistent with the measurement made by a optic probe.

We also present a symbolic token matching technique for the measurements of individual acrylic particle velocities, in which the points corresponding to the locations of particles are taken as the symbolic representation. In order to locate particles in images, several techniques are compared: synthetic discriminant function (SDF), minimum average correlation energy (MACE) filter, modified minimum average correlation energy (MMACE) filter and variance normalized correlation. We propose the MMACE filter,

which adjusts the amount of averaged spectrum of training images in the spectrum whitening stage of the MACE filter such that good generalization is achieved at the little expense of sharpness of peaks. We demonstrate that the performance of MMACE filter is very sensitive to the implementations and propose the best implementation from the viewpoint of good generalization and sharpness of peaks. MMACE filter is expected to work fairly well with images that have inconsistent brightness patterns of objects such as irregularly shaped particles if it is synthesized with considerable number of training images. Since the acrylic particles have the same spherical shapes, they do not cause distortions in the images involved in rotation. Thus, the acrylic particles are located with variance normalized correlation using a 2-D Gaussian function to extract the image data of a particle, followed by the clustering technique, which produces the point patterns. Then, the correspondence between point patterns is solved by the Hopfield network which is formulated as a constrained optimization. Five constraints in the energy function provide valid solutions to the correspondence problems; those are the constraints to legitimate solution for the permutation matrices (3 constraints), the minimization of sum of displacements for corresponding points and the rigidity constraint. The velocity measurements of acrylic particles are refined to the subpixel resolution by the correlation with the interpolation between image areas corresponding to matched points. Also, this method is evaluated with grid point patterns under ambiguous motions and with a rotating bumpy base sample.

Variance normalized correlation is applied to the images of flowing glass particles to measure the velocity and temperature for the steady and wavy flow. From the velocity variation monitored at the top of the flows, we find that the velocity in the steady flow changes randomly, whereas that in the wavy flow changes periodically. The qualitative

comparison of the experimental measurements with the theoretical model (Richman and Marciniec 1990) shows that the overall trend of the temperature profile in the theoretical model is different from that in the experimental measurements: the theory says that the temperature is generated at the bumpy boundary, whereas the experimental measurements say that the temperature is dissipated at the boundary. Also, we point out differences between the assumptions of the theoretical model and the experimental setup such as the dimension of the flows and the definition of the bumpiness. Thus, in order to quantitatively compare the experimental measurements with a theoretical model, the development of the model that conforms to the experimental setup is required.

We propose a method for the volume fraction measurement of acrylic particles, which is produced by counting particles in a well defined point pattern. Comparing with Drake's manual method, this method produces more reliable and accurate volume fraction measurement automatically.

APPENDIX A
DESCRIPTION OF IMAGING SYSTEM

We have used a KODAK EKTAPRO EM Motion Analyzer, Model 1012 which is composed of a imager, controller and processor. The imager has an image intensifier assembly. This increases the imager's ability to capture events in low light or to reduce the blurring of objects moving very rapidly. The intensified imager sends its video output to the processor and is connected to the controller. The controller provides power and control signals to the image intensifier assembly.

Main system features are summarized as follows:

* Sensor: 192 by 239 pixels NMOS array
* Gray Scale: 256 levels
* Record Rates: 50, 125, 250, 500 and 1, 000 full frames/ second
* Exposure: 1/ 50 to 1/ 12, 000 of a second
* Gate Limits: 10 microseconds to 5 milliseconds
* Gain Limits: 1 to 100
* Frame Storage: From 400 to 4, 800 full frame images (Our system: 818 frames)
* Play back Rates: NTSC: 0, 1, 2, 3, 3.8, 5, 6, 7.5, 10, 15, 30, 60, 90, 120, 240, 480, 960 frames/ second plus single step, freeze frame forward or reverse
* Signal Inputs: TRIGGER, EXT SYNC, ROC
* Video Output: System can be configured for either NTSC or PAL compatible output

The KODAK EKTAPRO Transfer Utility (EMUTILS) program provides a graphical user interface with the KODAK EKTAPRO EM Motion Analyzer. Using the program, a personal computer can control the Motion Analyzer. The program also imports digital video images in TIFF format from the Motion Analyzer and displays the images along with the DATA-FRAME Border information such as date, time and record rate at which the images are taken.

APPENDIX B
DESCRIPTION OF DEVELOPED PROGRAMS

As described in appendix A, the image file format from the camera is TIFF. Thus, the TIFF files are converted to RAW files (binary files). Then, C programs are developed for highly computational tasks and MATLAB programs are developed for mostly graphical representation of results from the C programs.

The developed program are classified according to context of this dissertation: the velocity and temperature measurement of flowing glass particles and the velocity and concentration measurement of flowing acrylic particles.

Velocity and Temperature Measurement of Flowing Glass Particles

Match31.c. This program provides the velocity measurement using the variance normalized correlation for side-view images. The images are divided into 14 by 17 blocks whose size is 13 by 13 pixels. Then, the best match for each block is found in a search area (11 by 11 pixels, up/ down 5 pixels and left 9/ right 1 pixel). Interpolation is applied to obtain the measurements with subpixel resolution of 1/ 10 pixel. The program requires to specify two successive image and output file names in order, in which the first image precedes the second image in time. The output file contains the 14 by 17 velocity measurements and correlation values.

Match32.c. This program is a counterpart of the Match31.c for top-view images. Its search area is 5 by 5 pixels (up/ down 2 pixels and left 3/ right 1 pixel).

Vector4.m. This program produces the velocity field from the output file of the Match31.c. A user-specified threshold checks the correlation values. If a correlation value exceeds the threshold, corresponding velocity is presented in the velocity field. Otherwise, velocities are set to zeros, which turn out to be points in the velocity field. The program also requires two scale factors and the location of the chute base in images. One scale factor is a ratio of the displacement (pixels/ frame) to the velocity (cm/ sec). The other scale factor is a ratio of the real size (cm) to the image size (pixels). The location of the chute base is referenced with respect to upper left corner of images, which leads to the flow height reference in the velocity field.

Vector41.m. This program is a counterpart of the Vector4.c for top-view images. The threshold and the two scale factors are required as in the Vector4.m.

Avelpr11.m. This program produces the velocity profile from the output file of the Match31.c. The velocity measurements are averaged for each row of corresponding velocity field. The velocity measurements whose correlation values are lower the user-specified threshold are not used in the average. The program also requires two scale factors and the location of the chute base in images as in the Vector4.m.

Avelpr12.m. This program produces the averaged velocity profile from 8 pairs of side-view images (8 output files of the Match31.c). The average is accomplished in the same manner as in the Avelpr11.m. Also, the temperature is measured by calculating sample variance of velocity measurements whose correlation values exceed the user-specified threshold. The program also requires two scale factors and the location of the chute base.

Avelpr14.m. This program is a counterpart of the Avelpr11.m for top-view images. The threshold and the two scale factors are required as in the Avelpr11.m.

Avelpr15.m. This program is a counterpart of the Avelpr12.m for top-view images. The threshold and the two scale factors are required as in the Avelpr12.m.

Velocity and Concentration Measurement of Flowing Acrylic Particles

Mmace33.m. This program produces the MMACE filter output for the acrylic particles as shown in chapter 3. The program can also produce either MACE filter output or SDF output depending on the value of α.

Vancorr21.c. This program locates acrylic particles using the variance normalized correlation and a clustering technique. The program produces a output file that contains particle coordinates (point pattern).

Pocor31.m. This program solves correspondence between point patterns using a Hopfield network. The point patterns are divided into blocks of 30 by 30 pixels with 10 pixels overlapped. The correspondence is updated as each block is evaluated.

Concent.m. This program produces the concentration measurement from a point pattern. The measurement provides the number of particles at each vertically divided image area by the particle size.

REFERENCES

Adelson, E. H.; Bergen, J. R. (1985) Spatiotemporal Energy Models for the Perception of Motion. J. Opt. Soc. Am. A., Vol. 2, No. 2, 284 - 299

Barnard, E.; Casasent, D. P. (1989) Multitarget Tracking with Cubic Energy Optical Neural Nets. App. Opt., Vol. 28, No. 4, 791 - 798

Bruck, J.; Goodman, J. W. (1988) A Generalized Convergence Theorem for Neural Networks. IEEE Trans. Inf. Theory, Vol. 34, No. 5, 1089 - 1092

Burt, P. J.; Yen, C.; Xu, X. (1982) Local Correlation Measures for Motion Analysis, a Comparative Study. IEEE Computer Society Conference on Pattern Recognition and Image Processing, Las Vegas, Nev., 269 - 274

Campbell C. S. (1990) Rapid Granular Flows. Annu. Rev. Fluid Mech., Vol. 22, 57 - 92

Casasent D. (1984) Unified Synthetic Discriminant Function Computational Formulation. App. Opt., Vol. 23, No. 10, 1620 - 1627

Daugman, J. G. (1989) Networks for Image Analysis: Motion and Texture. IJCNN, Vol. 1, 189 - 193

Drake, T. G. (1991) Granular Flow: Physical Experiments and Their Implications for Microstructural Theories. J. Fluid Mech., Vol. 225, 121 - 152

Glazer, F.; Reynolds, G.; Anandan, P. (1983) Scene Matching by Hierarchical Correlation. IEEE Computer Society Conference on Computer Vision and Pattern Recognition, Washington, D. C., 432 - 441

Hanes, D. M.; Inman, D. L. (1985) Observations of Rapidly Flowing Granular-Fluid Materials. J. Fluid Mech., Vol. 150, 357 - 380

Heeger, D. J. (1987) Model for the Extraction of Image Flow. J. Opt. Soc. Am. A., Vol. 4, No. 8, 1455 - 1471

Hopfield, J. J. (1982) Neural Networks and Physical Systems with Emergent Collective Computational Abilities. Proc. Natl. Acad. Sci. USA, Vol. 79, 2554 - 2558, Biophysics

Hopfield, J. J. (1984) Neurons with Graded Response have Collective Computational Properties like Those of Two-state Neurons. Proc. Natl. Acad. Sci. USA, Vol. 81, 3088 - 3092, Biophysics

Hopfield, J. J.; Tank, D. W. (1985) "Neural" Computation of Decisions in Optimization Problems. Biol. Cybern., Vol. 52, 141 - 152

Hopfield, J. J.; Tank, D. W. (1986) Computing with Neural Circuits: A Model. Science, Vol. 233, 625 - 633

Horn, B. K. P.; Schunck, B. G. (1981) Determining Optical Flow. Artif. Intell., Vol. 17, 185 - 203

Jenkins, J. T.; Savage, S. B. (1983) A Theory for the Rapid Flow of Identical, Smooth, Nearly Elastic, Spherical Particles. J. Fluid Mech., Vol. 130, 187 - 202

Johnson, P. C.; Nott, P.; Jackson, R. (1990) Frictional-Collisional Equations of Motion for Particulate Flows and Their Application to Chutes. J. Fluid Mech., Vol. 210, 501 - 535

Kahl, D. J.; Rosenfeld, A.; Danker, A. (1980) Some Experiments in Point Pattern Matching. IEEE Trans. Syst., Man, Cybern., Vol. SMC-10, No. 2, 105 - 115

Mahalanobis, A.; Kumar, B. V. K. V.; Casasent D. (1987) Minimum Average Correlation Energy Filters. App. Opt., Vol. 26, No. 17, 3633 - 3640

McCardle, J. (1993) Measurement of Particle Speed through Optical Reflective Sensing. Master's Thesis, University of Florida,

Musmann, H. G.; Pirsch, P.; Grallert, H. (1985) Advances in Picture Coding. Proc. IEEE, Vol. 73, No. 4, 523 - 548

Nasrabadi, N. M.; Choo, C. Y. (1992) Hopfield Network for Stereo Vision Correspondence. IEEE Trans. Neural Networks, Vol. 3, No. 1, 5 - 13

Pao, Y. (1989) Adaptive Pattern Recognition and Neural Networks. Massachusetts, Addison-Wesley

Patrose, B.; Caram, H. S. (1982) Optical Fiber Probe Transit Anemometer for Particle Velocity Measurements in Fluidized Beds. AIChE J., Vol. 28, 604 - 609

Prager, J. M.; Arbib, M. A. (1983) Computing the Optical Flow: the MATCH Algorithm and Prediction. Comput. Vision, Graphics, Image Process., Vol. 24, 271 - 304

Ranade, S.; Rosenfeld, A. (1980) Point Pattern Matching by Relaxation. Pattern Recognit., Vol. 12, 269 - 275

Richman, M. W.; Marciniec R. P. (1990) Gravity-Driven Granular Flows of Smooth, Inelastic Spheres Down Bumpy Inclines. J. Appl. Mech. Trans. ASME, Vol. 57, 1036 - 1043

Rosenfeld, A.; Kak, A. C. (1976) Digital Picture Processing. New York, Academic Press

Savage, S. B. (1979) Gravity Flow of Cohesionless Granular Materials in Chutes and Channels. J. Fluid Mech., Vol. 92, part 1, 53 - 96

Schunck, B. G. (1989) Image Flow Segmentation and Estimation by Constraint Line Clustering. IEEE Trans. Pattern Anal. Mach. Intell., Vol. 11, No. 10, 1010 - 1027

Tsai, W. H.; Fu, K. S. (1979) Error-Correcting Isomorphisms of Attributed Relational Graphs for Pattern Analysis. IEEE Trans. Syst., Man, Cybern., Vol. SMC-9, 757-768

Tsao, T.; Chen, V. C. (1991) A Neural Network Based on Differential Gabor Filters for Computing Image Flow from Two Successive Images. IJCNN, Vol. 1, 741 - 748

Watson, A. B.; Ahumada, A. J. (1985) Model of Human Visual-Motion Sensing. J. Opt. Soc. Am. A., Vol. 2, No. 2, 322 - 342

Xie, C. G.; Stott, A. L.; Huang, S. M.; Plaskowski, A; Beck, M. S. (1989) Mass-Flow Measurement of Solids using Electrodynamic and Capacitance Transducers. J. Phys. E: Sci. Instrum. Vol. 22, 712 - 719

BIOGRAPHICAL SKETCH

Jingeol Lee was born February 26, 1958 in Busan, Korea. He received the bachelor's degree and master's degree in electronic engineering from Korea University, Seoul in 1981 and 1985, respectively.

From 1982 to 1990, he had worked at the Agency for Defense Development, Jinhae, Korea where he was a researcher. At the Agency for Defense Development, he was awarded the Defense Development Silver Prize from the Agency for Defense Development and the Defense Development Encouragement from the Department of Defense in recognition of R&D achievement in 1989 and 1990, respectively.

In January 1991, he started a Ph. D. program in electrical engineering, University of Florida, where he has studied digital signal processing.